

The effects of a hot gaseous halo in galaxy major mergers

Benjamin P. Moster^{1,2} ^{*}, Andrea V. Macciò¹, Rachel S. Somerville^{3,4},
 Thorsten Naab², T. J. Cox⁵

¹ Max-Planck-Institut für Astronomie, Königstuhl 17, 69117 Heidelberg, Germany

² Max-Planck Institut für Astrophysik, Karl-Schwarzschild Straße 1, 85748 Garching, Germany

³ Space Telescope Science Institute, Baltimore MD 21218

⁴ Department of Physics and Astronomy, Johns Hopkins University, Baltimore MD 21218

⁵ Carnegie Observatories, 813 Santa Barbara Street, Pasadena, CA 91101, USA

18 January 2013

ABSTRACT

Cosmological hydrodynamical simulations as well as observations indicate that spiral galaxies are comprised of five different components: dark matter halo, stellar disc, stellar bulge, gaseous disc and gaseous halo. While the first four components have been extensively considered in numerical simulations of binary galaxy mergers, the effect of a hot gaseous halo has usually been neglected even though it can contain up to 80% of the total gas within the galaxy virial radius. We present a series of hydrodynamic simulations of major mergers of disc galaxies, that for the first time include a diffuse, rotating, hot gaseous halo. Through cooling and accretion, the hot halo can dissipate and refuel the cold gas disc before and after a merger. This cold gas can subsequently form stars, thus impacting the morphology and kinematics of the remnant. Simulations of isolated systems with total mass $M \sim 10^{12} M_{\odot}$ show a nearly constant star formation rate of $\sim 5 M_{\odot} \text{ yr}^{-1}$ if the hot gaseous halo is included, while the star formation rate declines exponentially if it is neglected. We conduct a detailed study of the star formation efficiency during mergers and find that the presence of a hot gaseous halo reduces the starburst efficiency ($e = 0.5$) compared to simulations without a hot halo ($e = 0.68$). The ratio of the peak star formation rate in mergers compared to isolated galaxies is reduced by almost an order of magnitude (from 30 to 5). Moreover we find cases where the stellar mass of the merger remnant is lower than the sum of the stellar mass of the two progenitor galaxies when evolved in isolation. This suggests a revision to semi-analytic galaxy formation models which assume that a merger always leads to enhanced star formation. In addition, the bulge-to-total ratio after a major merger is decreased if hot gas is included in the halo, due to the formation of a more massive stellar disc in the remnant. We show that adding the hot gas component has a significant effect on the kinematics and internal structure of the merger remnants, like an increased abundance of fast rotators and an $r^{1/4}$ surface brightness profile at small scales. The consequences on the population of elliptical galaxies formed by disc mergers are discussed.

Key words: galaxies: elliptical, evolution, haloes, interactions, starburst, structure – methods: numerical, N-body simulation

1 INTRODUCTION

Galaxy mergers, both major (near-equal mass) and minor (unequal mass), are a generic prediction of structure assembly in the Cold Dark Matter (CDM) model (e.g. White & Rees 1978; Davis et al. 1985). Mergers are an important component of the modern theory of galaxy forma-

tion and are thought to be a significant physical driver of many galaxy properties. Major mergers can transform disc-dominated galaxies into spheroidals (Toomre 1977; Negro-ponte & White 1983; Hernquist 1992; Naab & Burkert 2003; Cox et al. 2006c), enhance star formation (Larson & Tinsley 1978; Kennicutt et al. 1987; Barnes & Hernquist 1991; Mihos & Hernquist 1994, 1996; Barton Gillespie et al. 2003; Cox et al. 2008) and possibly trigger Active Galactic Nuclei (AGN) activity (Sanders et al. 1988; Hernquist 1989;

^{*} moster@mpia.de

Springel et al. 2005; Hopkins et al. 2006; Johansson et al. 2009a; Younger et al. 2009; Debuhr et al. 2010, 2011). Minor mergers can thicken the galactic disc (Quinn et al. 1993; Velazquez & White 1999; Brook et al. 2004; Bournaud et al. 2005; Kazantzidis et al. 2008; Villalobos & Helmi 2008; Read et al. 2008; Purcell et al. 2009; Moster et al. 2010) and create a diffuse stellar halo (Murante et al. 2004; Bullock & Johnston 2005; Bell et al. 2008; Murante et al. 2010). Observations find large samples of recent merger remnants in the local universe (Schweizer 1982; Lake & Dressler 1986; Doyon et al. 1994; Shier & Fischer 1998; Genzel et al. 2001; Dasyra et al. 2006) and that $\sim 5 - 10\%$ of low- and intermediate-mass galaxies are in the process of merging (Bridge et al. 2010). An average $\sim M_*$ galaxy has experienced about one major merger since $z \sim 2 - 3$ (Bridge et al. 2007; Kartaltepe et al. 2007; Conselice et al. 2008; Lin et al. 2008; Lotz et al. 2008; Conselice et al. 2009; Jogee et al. 2009).

Since the “merger hypothesis” was proposed by Toomre & Toomre (1972) there have been many publications on numerical simulations studying the dynamics of galaxy mergers and the properties of merger remnants (Gerhard 1981; Negroponte & White 1983; Barnes 1988; Hernquist 1993; Barnes & Hernquist 1996; Di Matteo et al. 2005; Naab & Trujillo 2006; Cox et al. 2006b; Jesseit et al. 2007; Hoffman et al. 2009). In recent years several groups have produced very large libraries of major merger simulations, considering different orbital parameters of the merger, the effect of the implemented gas physics, and different star formation algorithms and feedback schemes (Robertson et al. 2006b; Cox et al. 2006c; Naab et al. 2006; Bois et al. 2010). One clear outcome of those simulations has been the need to include gas physics in order to reproduce basic properties of observed galaxies. Gas plays an important role in shaping the properties of galaxy mergers and their remnants, because unlike stars and dark matter, gas can cool radiatively and therefore lose kinetic energy efficiently. Furthermore, gas can lose angular momentum due to gravitational torques during merger events. After the merger, an extended cold gas disc can form in the remnant from high angular momentum gas in the outer regions of the progenitors. By the accumulation of cold gas in the centre of a merger remnant the central potential changes impacting the orbital configuration of the stars (Barnes & Hernquist 1996). Additionally, the gas is eventually transformed into stars, leading to a new stellar component which is rotating and kinematically cold. It has been shown that in numerical simulations even major mergers of disc galaxies can produce remnants with large discs if the cold gas fractions in the progenitors are sufficiently high (Barnes 2002; Springel & Hernquist 2005; Robertson et al. 2006a; Naab et al. 2006; Governato et al. 2007, 2009). This has also been seen in observations of high-redshift discs that are probably reforming after mergers (van Dokkum et al. 2004; Kassin et al. 2007; Genzel et al. 2008; Puech et al. 2008).

Detailed studies of elliptical galaxies indicate that they can be classified into two groups with respect to their structural properties (Davies et al. 1983; Bender 1988; Bender & Nieto 1990; Kormendy & Bender 1996). Low and intermediate mass giant elliptical galaxies exhibit significant rotation along the photometric major axis (see e.g. Emsellem et al. 2007, 2011). Although their rotation is broadly consistent with models of isotropic rotators it has been demonstrated

by Cappellari et al. (2007) and Emsellem et al. (2011) that rotating ellipticals are intrinsically more anisotropic than slowly rotating massive ellipticals. This finding is in agreement with disc merger simulations (Burkert et al. 2008). The isophotes of rotating ellipticals tend to be discy. They have power-law surface brightness profiles (Lauer et al. 1995; Faber et al. 1997) and show little or no radio and X-ray emission (Bender et al. 1989). Large, luminous spheroids, on the other hand, have box-shaped isophotes, show flat cores and strong radio and X-ray emission. They rotate slowly, exhibit kinematically decoupled components, and have a large amount of minor-axis rotation (see Cappellari et al. 2011; Emsellem et al. 2011; Krajnović et al. 2011, for recent results from the ATLAS^{3D} survey).

The different physical properties of elliptical galaxies lead to the viewpoint that the two classes have different formation histories and form through different mechanisms. Many studies find that collisionless merger simulations lead to slowly rotating, pressure supported, anisotropic remnants (Negroponte & White 1983; Barnes 1988; Hernquist 1992). Along this line of reasoning, Naab et al. (1999), Bendo & Barnes (2000) and Naab & Burkert (2003) argue that fast rotating low luminosity ellipticals are produced by dissipationless minor mergers. However, remnants of dissipationless disc galaxies are in conflict with observations, as they do not have de Vaucouleurs profiles in the inner parts. The reason for this is that low phase-space density spirals cannot produce the high central phase-space densities of ellipticals — according to Liouville’s theorem, phase-space density is conserved during a collisionless process (Carlberg 1986). This problem could only be overcome in dissipationless simulations by including large bulge components in the progenitor systems (Hernquist et al. 1993; Naab & Trujillo 2006).

Another way to circumvent this problem is to take into account the gas component in the progenitors, which can increase the phase-space density through radiation (Lake 1989). It has been argued by Kormendy & Bender (1996) and Faber et al. (1997) that the observed stellar discs embedded in rotating ellipticals (Rix & White 1990; Ferrarese et al. 1994; Scorza et al. 1998; Rix et al. 1999; Lauer et al. 2005; Krajnović et al. 2008) experienced dissipation during their formation while non-rotating systems would form from pure dissipationless mergers. This idea has been explored by several studies (Bekki & Shioya 1997; Bekki 1998; Naab et al. 2006; Jesseit et al. 2009; Hopkins et al. 2008, 2009b,c,d). Focusing on equal mass mergers, Cox et al. (2006b) confirmed that slowly rotating anisotropic spheroids can be formed in dissipationless simulations. Furthermore they show that if a massive gaseous disc is included in the progenitors, a consistent fraction of merger orbits leads to systems with significant rotation. Those remnants are able to reproduce the observed distribution of projected ellipticities, rotation parameters and isophotal shapes. One open issue is that these results rely on a relatively high (possibly too high) gas content in the discs of the merger progenitors and that only a fraction of the considered orbits lead to fast rotators. It remains unclear whether the abundance of disc galaxies with such gas fractions is high enough in order to explain the large number of fast rotating elliptical galaxies observed in the local universe (de Zeeuw et al. 2002; Emsellem et al. 2007; Cappellari et al. 2007; Emsellem et al. 2011).

The initial conditions for almost all hydrodynamic sim-

ulations of galaxy mergers performed so far have considered only cold gas that is present within the progenitor discs at the start of the simulation. However, semi-analytic models of galaxy formation (Kauffmann et al. 1993; Bower et al. 2006; De Lucia & Blaizot 2007; Monaco et al. 2007; Somerville et al. 2008b) as well as full cosmological hydrodynamic simulations (e.g. Toft et al. 2002; Sommer-Larsen 2006; Johansson et al. 2009b; Rasmussen et al. 2009; Stinson et al. 2010; Hansen et al. 2010) both predict a large amount of hot gas in quasi-hydrostatic equilibrium within the gravitational potential of the dark matter halo. Smooth accretion of gas from these haloes can grow the discs of spiral galaxies (Abadi et al. 2003; Sommer-Larsen et al. 2003; Guo & White 2008). As the gas mainly cools via thermal bremsstrahlung it radiates primarily in the soft X-ray band.

Since this halo X-ray luminosity depends on the mass of the system, observational studies are naturally biased towards very massive haloes. Hence, hot gas in massive ellipticals has been observed in galaxy groups and clusters and in isolated systems (see Mathews & Brightenti 2003, and references therein). In smaller haloes, however, the gas temperature can be lower than 10^6 K and thus difficult to observe with current X-ray telescopes, as the radiation is only detectable in very soft bands. Still, studies performed in the last few years have identified X-ray emission from diffuse hot gas in various energy bands (Benson et al. 2000; Wang et al. 2003; Strickland et al. 2004; Wang 2005; Tüllmann et al. 2006; Li et al. 2007; Sun et al. 2009; Owen & Warwick 2009). In the MW, X-ray absorption lines produced by local hot gas have been detected in the spectra of several AGN. Sembach et al. (2003) and Tripp et al. (2003) have argued that this emission comes from the interface between warm clouds and the ambient hot medium. Given the existence of hot gaseous haloes around galaxies, it is important to include these in simulations of isolated galaxies and mergers.

In the last few years there have been several studies that have taken a gaseous halo into account. Mastropietro et al. (2005) and Mastropietro et al. (2009) employ a hot halo component to study the hydrodynamic and gravitational interaction between the Large Magellanic Cloud and the MW. Sinha & Holley-Bockelmann (2009) ran merger simulations of galaxies consisting of dark matter and hot halo gas in order to study the change of temperature and X-ray luminosity induced by shocks during the mergers. Those studies, however, use adiabatic simulations, neglecting cooling and star formation. Focusing on isolated systems, Kaufmann et al. (2006) and Kaufmann et al. (2009) simulated systems consisting of a dark matter and a hot halo component to study the evolution and cooling behaviour of the hot halo and the formation of discs via cooling flows. Similarly, Viola et al. (2008) ran simulations of a gas halo embedded in a dark matter halo to study the cooling process and assess how well simple models can represent it. So far, no study has included a rotating, cooling gaseous halo in merger simulations.

The goal of this paper is to test the impact of including such a large gas reservoir on star formation and remnant properties in major mergers of disc galaxies. For the first time we include a gradually cooling hot gas halo (as expected in a cosmological context) in our galaxy models. We present a detailed analysis of the effects of this new gas component and focus our attention on three main quantities: the star

formation efficiency during and after the merger, and the morphology and kinematics of merger remnants.

The paper is organized as it follows: in section 2 we provide a brief summary of the GADGET-2 code and the initial conditions. We also explain how the initial conditions have been set up to include a rotating hot gaseous halo, and show the results of simulations constraining the initial spin of this hot halo. In section 3 we present our main results for the major merger simulations, focusing on the differences between the simulations with and without a hot gaseous component. We present star formation rates, starburst efficiencies and structural and kinematic properties of the remnants. Finally, in section 4 we summarize and discuss our results and compare them to previous studies that have neglected the gaseous halo.

2 NUMERICAL SIMULATIONS

2.1 Numerical Code

All numerical simulations in this work were performed using the parallel TreeSPH-code GADGET-2 (Springel 2005). Gas dynamics is followed with the Lagrangian smoothed particle hydrodynamics (SPH Lucy 1977; Gingold & Monaghan 1977; Monaghan 1992; Springel 2010) technique, employed in a formulation that manifestly conserves energy and entropy (Springel & Hernquist 2002). Radiative cooling is implemented for a primordial mixture of hydrogen and helium following Katz et al. (1996), with a spatially uniform time-independent local photo-ionizing UV background in the optically thin limit (Haardt & Madau 1996).

For modelling star formation and the associated heating by supernovae (SN) we follow the sub-resolution multiphase ISM model developed by Springel & Hernquist (2003). In this model, a thermal instability is assumed to operate above a critical density threshold ρ_{th} , producing a two-phase medium which consists of cold clouds embedded in a tenuous gas at pressure equilibrium. Stars are formed from the cold clouds on a timescale chosen to match observations (Kennicutt 1998) and short-lived stars supply an energy of 10^{51} ergs to the surrounding gas as supernovae. This energy heats the diffuse phase of the ISM and evaporates cold clouds, such that a self-regulated cycle for star formation is established. The threshold density ρ_{th} is determined self-consistently by demanding that the equation of state (EOS) is continuous at the onset of star formation. In a subset of simulations we include SN-driven galactic winds as proposed by Springel & Hernquist (2003). In this model the mass-loss rate carried by the wind is proportional to the star formation rate (SFR) $M_w = \eta \dot{M}_*$, where the mass-loading-factor η quantifies the wind efficiency. Furthermore, the wind is assumed to carry a fixed fraction of the supernova energy, such that there is a constant initial wind speed v_w (energy-driven wind).

We adopt the standard parameters for the multiphase model in order to match the Kennicutt Law as specified in Springel & Hernquist (2003). The star formation timescale is set to $t_*^0 = 2.1$ Gyr, the cloud evaporation parameter to $A_0 = 1000$ and the SN “temperature” to $T_{SN} = 10^8$ K. We employ a Salpeter (1955) initial mass function (IMF) which sets the mass fraction of massive stars $\beta = 0.1$. For the galactic winds we adopt a mass-loading factor of $\eta = 2$ which is

Table 1. Parameters kept constant for all simulations. Masses are in units of $10^{10} M_{\odot}$, scale and softening lengths are in units of kpc and pc, respectively

System	M_{dm}	M_{b}	r_{d}	r_{g}	r_{b}	z_0	c	λ	N_{dm}	N_{bulge}	ϵ_{DM}	ϵ_{stars}
Z1	80	0.500	2.50	3.75	0.50	0.6	3.64	0.030	500 000	20 000	400	100
G3	110	0.890	2.85	8.55	0.62	0.4	6.00	0.050	240 000	20 000	400	100

motivated by observations (Martin 1999; Rupke et al. 2005; Martin 2005), and a wind speed of $v_w \sim 480 \text{ km s}^{-1}$, typical for a Milky Way (MW)-like galaxy at low redshift. We do not include feedback from accreting black holes (AGN feedback) in our simulations.

2.2 Galaxy Models

To construct the galaxy models used in our simulations we apply and extend the method described in Springel et al. (2005). Each system is composed of a cold gaseous disc, a stellar disc and a stellar bulge with masses M_{cg} , M_{disc} and M_{b} embedded in a halo that consists of hot gas and dark matter with masses M_{hg} and M_{dm} .

The gaseous and stellar discs are rotationally supported and have exponential surface density profiles. The scale length of the gaseous disc r_{g} is related to that of the stellar disc r_{d} by $r_{\text{g}} = \chi r_{\text{d}}$. The vertical structure of the stellar disc is described by a radially independent sech^2 profile with a scale height z_0 , and the vertical velocity dispersion is set equal to the radial velocity dispersion. The gas temperature is fixed by the EOS, rather than the velocity dispersion. The vertical structure of the gaseous disc is computed self-consistently as a function of the surface density by requiring a balance of the galactic potential and the pressure given by the EOS. The spherical stellar bulge is non-rotating and is constructed using the Hernquist (1990) profile with a scale length r_{b} . The dark matter halo has a Hernquist (1990) profile with a scale length r_{s} , a concentration parameter $c = r_{\text{vir}}/r_{\text{s}}$ and a halo spin λ .

2.2.1 Modelling the hot gaseous halo

For MW-like galaxies there are no existing observations that constrain the profile of the gaseous hot halo. Therefore, we choose the observationally motivated β -profile (Cavaliere & Fusco-Femiano 1976; Jones & Forman 1984; Eke et al. 1998) which is commonly used to describe hot gas in galaxy clusters:

$$\rho_{\text{hg}}(r) = \rho_0 \left[1 + \left(\frac{r}{r_c} \right)^2 \right]^{-\frac{3}{2}\beta} \quad (1)$$

It has three free parameters: the central density ρ_0 , the core radius r_c and the outer slope parameter β . The temperature profile can be fixed by assuming isotropy and hydrostatic equilibrium inside the galactic potential. The halo temperature at a given radius r is then determined by the cumulative mass distribution $M(r)$ of the dark matter, stellar and gaseous components beyond r and by the density profile $\rho_{\text{hg}}(r)$ of the hot gas:

$$T(r) = \frac{\mu m_p}{k_B} \frac{1}{\rho_{\text{hg}}(r)} \int_r^{\infty} \rho_{\text{hg}}(r') \frac{GM(r')}{r'^2} dr , \quad (2)$$

where m_p is the proton mass, G and k_B are the gravitational and Boltzmann constants and μ is the mean molecular weight.

In addition the hot gaseous halo is rotating around the spin axis of the disc. The angular momentum of the hot gaseous halo is set by requiring that the specific angular momentum of the the gas $j_{\text{hg}} = J_{\text{hg}}/M_{\text{hg}}$ is a multiple of the specific angular momentum of the dark matter halo $j_{\text{dm}} = J_{\text{dm}}/M_{\text{dm}}$ such that $j_{\text{hg}} = \alpha j_{\text{dm}}$. A value of $\alpha = 1$ matches the commonly adopted assumption that there is no angular momentum transport between the spherical dark matter halo and the gaseous halo. The angular momentum distribution is then assumed to scale with the product of the cylindrical distance from the spin axis R and the circular velocity at this distance: $j(R) \propto R v_{\text{circ}}(R)$. The vertical velocity of the gas halo particles is set equal to zero.

2.2.2 Parameters of the gaseous halo

The hot gaseous halo is then described by four parameters: the central density ρ_0 , the core radius r_c , the slope parameter β and the spin factor α . For the density profile, we adopt $\beta = 2/3$ (Jones & Forman 1984) and $r_c = 0.22r_s$ (Makino et al. 1998). Thus there is a central core with a constant density and the slope in the outer halo is -2 .

In order to demonstrate the maximum effect that the hot gaseous halo can have, we fix ρ_0 such that the baryonic fraction within r_{vir} (stellar and gaseous discs, bulge and gaseous halo) is the universal value, as this is the maximum fraction that a gaseous halo can achieve. We also test an intermediate case, where we adopt only half of this maximal hot gas mass to investigate whether the results fall between the extreme cases (no and maximal gaseous halo). The results of this test are presented in section 3.4. Note, however, that even for our maximum hot gaseous halo mass we do not violate constraints from X-ray observations; see section 4 for a more detailed discussion of this point.

This leaves one key free parameter which needs to be constrained, the spin factor α . In high resolution cosmological simulations one finds that at low redshift ($z \lesssim 2$) α is generally larger than 1, as feedback processes preferentially remove low angular momentum material from the halo (Governato et al. 2010).

In order to fix the spin factor for MW-like galaxies we model a typical MW-like galaxy at $z = 1$ and let it evolve to $z = 0$ using different values for α . We then employ two observational constraints (stellar mass and disc size) to determine the correct α . A typical MW-like galaxy with $M_{\text{dm}}(z = 0) \sim 10^{12} M_{\odot}$ has a halo concentration of

Table 2. Parameters for the different simulation runs. Masses are in units of $10^{10} M_{\odot}$, and softening lengths are in units of pc.

Run	f_{gas}	M_{disc}	M_{cg}	M_{hg}	α	N_{disc}	N_{cg}	N_{hg}	ϵ_{gas}	θ
Z1	0.40	2.00	1.33	0.0	-	100 000	33 333	0	140	-
Z1A1	0.40	2.00	1.33	12.0	1	100 000	33 333	375 000	140	-
Z1A2	0.40	2.00	1.33	12.0	2	100 000	33 333	375 000	140	-
Z1A4	0.40	2.00	1.33	12.0	4	100 000	33 333	375 000	140	-
Z1A8	0.40	2.00	1.33	12.0	8	100 000	33 333	375 000	140	-
G3	0.23	4.11	1.20	0.0	-	100 000	15 000	0	140	30°
G3f0	0.00	5.31	0.00	0.0	-	130 000	0	0	-	30°
G3f4	0.40	3.20	2.11	0.0	-	80 000	25 000	0	140	30°
G3f8	0.80	1.07	4.24	0.0	-	30 000	50 000	0	140	30°
G3h	0.23	4.11	1.20	11.0	4	100 000	15 000	175 000	140	30°
G3hf0	0.00	5.31	0.00	11.0	4	130 000	0	175 000	140	30°
G3hf4	0.40	3.20	2.11	11.0	4	80 000	25 000	175 000	140	30°
G3hf8	0.80	1.07	4.24	11.0	4	30 000	50 000	175 000	140	30°
G3hX	0.23	4.11	1.20	5.5	4	100 000	15 000	87 500	140	30°

$c = 8.43$ at $z = 0$ (Macciò et al. 2008) which fixes both parameters of the Hernquist profile. Assuming that the halo profile does not change from $z = 1$ to the present, we can compute the virial mass and the halo concentration given the higher background density at $z = 1$, resulting in $M_{\text{dm},z=1} = 8.0 \times 10^{11} M_{\odot}$ and $c_{z=1} = 3.64$. Using the redshift-dependent stellar-to-halo mass relation derived by Moster et al. (2010), converted to a Salpeter IMF, we assign a stellar mass of $M_{*,z=1} = 2.5 \times 10^{10} M_{\odot}$ to the system. Distributing 80% of this stellar mass into the exponential disc yields a stellar disc mass of $M_{\text{disc}} = 2.0 \times 10^{10} M_{\odot}$ and a bulge mass of $M_{\text{b}} = 5 \times 10^9 M_{\odot}$. A bulge scale length of $r_{\text{b}} = 0.5$ kpc is assumed. In order to determine the mass of the gaseous disc we use the recipe by Stewart et al. (2009) which is based on data by McGaugh (2005) and Erb et al. (2006). This recipe predicts that central galaxies with $M_* = 2.5 \times 10^{10} M_{\odot}$ at $z = 1$ have a gas fraction of $f_{\text{gas}} = M_{\text{cg}}/(M_{\text{cg}} + M_{\text{disc}}) = 0.4$ which yields a mass for the gaseous disc of $M_{\text{cg}} = 1.33 \times 10^{10} M_{\odot}$. The scale length for the stellar disc at $z = 1$ is set to $r_{\text{d}} = 2.4$ kpc, consistent with observations from GEMS (Barden et al. 2005; Somerville et al. 2008a), and corresponds to a spin parameter of $\lambda = 0.03$ assuming the scalings of Mo et al. (1998). We assume that the scale length of the gaseous disc r_{g} is a factor of $\chi = 1.5$ larger. The scale height of the stellar disc is set to $z_0 = 0.6$ kpc, typical for MW-like galaxies (Schwarzkopf & Dettmar 2000; Yoachim & Dalcanton 2006). The mass of the hot gaseous halo within r_{vir} is $M_{\text{hg}} = 1.2 \times 10^{11} M_{\odot}$, such that the baryonic fraction within r_{vir} is the universal value. The system is modeled with $N_{\text{dm}} = 500,000$ dark matter, $N_{\text{disc}} = 100,000$ stellar disc, $N_{\text{cg}} = 33,333$ gaseous disc, $N_{\text{bulge}} = 20,000$ bulge and $N_{\text{hg}} = 375,000$ gaseous halo particles. We set the gravitational softening length to $\epsilon = 100$ pc, 140 pc and 400 pc for stellar, gas and dark matter particles, respectively. We summarize the parameters that are kept constant for all simulations in Table 1, and parameters that differ for the various simulation runs are summarized in Table 2.

In order to fix the angular momentum of the gaseous halo, we run five simulations with different values of the spin

factor α . These include: one simulation with no gaseous halo at all (Z1), and simulations with $\alpha = 1, 2, 4$ and 8 (Z1A1, Z1A2, Z1A4, Z1A8). We evolve these simulations in isolation from $z = 1$ to $z = 0$ which corresponds to 7.6 Gyr. The simulations include stellar winds. For every time-step of the simulation we measure the virial mass of the dark matter halo (given the background density at this epoch) and use the empirical stellar-to-halo mass constraints derived by Moster et al. (2010) at that redshift to compute the mean stellar mass expected for this halo mass. We compare this to the stellar mass measured in the simulation. We also compute the radial density profile of the stellar disc and measure the exponential scale length. These values are compared to the mean observed scale length for disc galaxies of corresponding stellar mass at the given redshift (Barden et al. 2005; Somerville et al. 2008a). For example, the considered halo has a virial mass of $M_{\text{dm}} = 0.9 \times 10^{12} M_{\odot}$ at $z = 0.4$. The mean stellar mass of galaxies in a halo of this mass at this redshift is $M_* = 4 \times 10^{10} M_{\odot}$ and the mean observed scale length for galaxies of this stellar mass is $r_{\text{d}} = 2.82$ kpc. We require that the stellar mass and scale length measured in the simulations should obey these constraints.

We show the results of the simulations in Figure 1. For the simulation without a gaseous halo the evolution of the scale length agrees well with the observed values at $z \gtrsim 0.4$, while after that it does not grow rapidly enough and ends up being too small. The stellar mass evolution, however, completely disagrees with that of a typical galaxy of this halo mass. The reason for this is the lack of cold gas from which stars can form. As the initial cold gaseous disc is depleted quickly, but does not get refuelled from an external reservoir, there is not enough gas available to increase the disc mass by a factor of two by $z = 0$. This shows that the hot gaseous halo is very important in order to reproduce the SF history of spiral galaxies like our MW, by providing an extended supply of cold gas that can fuel ongoing star formation.

The simulations including a gaseous halo show a much larger SFR, with the value depending on the initial spin factor α . For low values of $\alpha = 1$ and 2, the stellar mass of the galaxy increases too fast and becomes too large at $z = 0$,

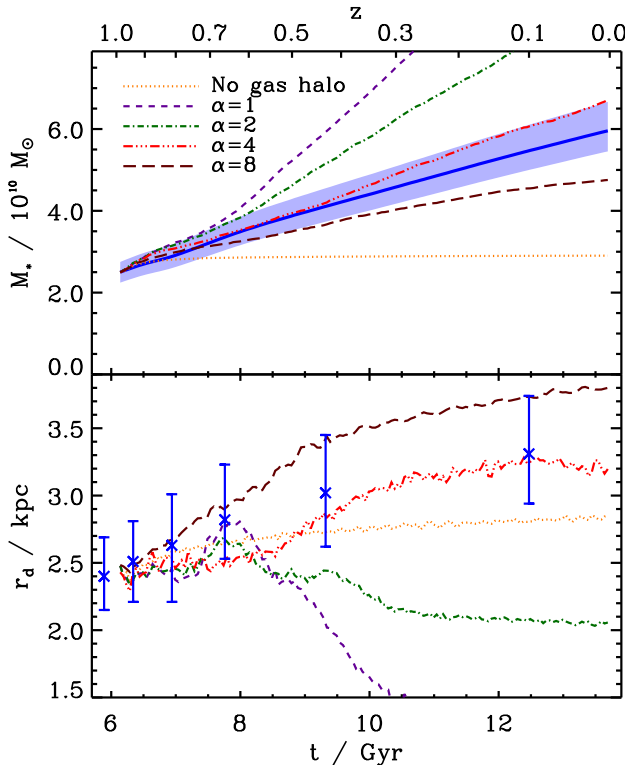


Figure 1. *Upper panel:* Stellar mass as a function of time for different values of the spin parameter for the hot gas halo α . The values measured in the simulations (lines) are compared to the observational constraints from Moster et al. (2010, bold line and shaded area). *Lower panel:* Disc scale length as function of time for different α . Symbols show the observed values by Barden et al. (2005). Only the simulation with $\alpha = 4$ agrees well with both constraints.

while the scale length quickly decreases and reaches values that are much smaller than the observed ones. These effects are due to the low angular momentum of the halo gas at the start of the simulation. When the gas cools, it is no longer supported by pressure, but only by angular momentum. This means that a lower initial angular momentum results in a lower orbital distance and thus in a lower scale length. Additionally, since the centrifugal barrier is lower, much more material can reach densities where SF is active which yields a much higher SFR and thus a larger stellar mass. For values of $\alpha \lesssim 3$, too much material concentrates at small distances from the galactic centre which results in overly massive and too compact discs compared to observations. On the other hand, large values of $\alpha = 8$ yield a stellar disc which is not massive enough and which has a scale length that is too large. Due to the larger initial angular momentum the cooling gas can retain large orbital distances. This also leads to much less dense star-forming material and thus to lower stellar masses. For values of $\alpha \gtrsim 6$, we find that gas settles in discs that are too large and does not form enough stars compared to observations.

The model that agrees best with the observational constraints is the one with a spin factor of $\alpha = 4$. For this value we find a stellar mass and a scale length which are consistent with the observational constraints for MW-like galaxies. As

a result we use this value throughout the rest of this paper for all systems, which are all in the halo mass range of the Milky-Way. We note that different values of α (representing different merger histories, feedback efficiencies, etc.) can easily result in a range of stellar masses and scale length, in agreement with the spread of these quantities for observed spiral galaxies.

2.3 Merger Simulation Parameters

To study equal mass mergers of disc galaxies we adopt the galaxy model G3 used by Cox et al. (2008), which is tuned to match SDSS observations of local spirals. The stellar mass of this galaxy was chosen to be $M_* = 5 \times 10^{10} M_\odot$. The bulge-to-disc ratio of $B/D = 0.22$ is taken from de Jong (1996), resulting in a stellar disc mass of $M_{\text{disc}} = 4.11 \times 10^{10} M_\odot$ and a bulge mass of $M_b = 8.9 \times 10^9 M_\odot$. The gas fraction in the disc of 0.23 is motivated by the gas-to-stellar mass scaling relation from Bell et al. (2003) and yields a mass for the cold gaseous disc of $M_{\text{cg}} = 1.2 \times 10^{10} M_\odot$. The sizes of the stellar disc and bulge were chosen to agree with the stellar mass-size relation of Shen et al. (2003) resulting in $r_d = 2.85$ kpc and $r_b = 0.62$ kpc. The scale length of the gaseous disc was assumed to be a factor of $\chi = 3$ larger than that of the stellar disc, such that $r_g = 8.55$. The scale height of the stellar disc was set to $z_0 = 0.4$ kpc. The mass and concentration of the dark matter halo were selected such that the rotation curves lie on the baryonic Tully-Fisher relation (Bell & de Jong 2001; Bell et al. 2003) which yields a virial mass of $M_{\text{dm}} = 1.1 \times 10^{12} M_\odot$ and a concentration parameter of $c = 6$. In order to explore the effects of different initial progenitor gas fractions on starbursts and remnant morphologies we construct additional galaxy models with modified disc gas fractions of 0%, 40% and 80% (G3f0, G3f4 and G3f8). In some simulations we extend this model to also include a hot gaseous halo (G3hf0, G3h, G3hf4, G3hf8) with a mass of $M_{\text{hg}} = 1.1 \times 10^{11} M_\odot$ within r_{vir} and a hot gas spin factor of $\alpha = 4$. In addition, we construct a system with only half of the maximal hot gas mass, i.e. $M_{\text{hg}} = 5.5 \times 10^{10} M_\odot$ within r_{vir} (G3hX). We set the gravitational softening length to $\epsilon = 100$ pc, 140 pc and 400 pc for stellar, gas and dark matter particles, respectively.

We follow Cox et al. (2008) and choose a nearly unbound elliptical orbit with an eccentricity of $e_{\text{orbit}} = 0.95$, a pericentric distance of $r_{\text{min}} = 13.6$ kpc and an initial separation of $d_{\text{start}} = 250$ kpc¹. The resulting interactions are fast and nearly radial, consistent with merger orbits found in cosmological N -body simulations (Benson 2005; Khochfar & Burkert 2006). We employ a prograde orbit; the spin axes of the first galaxy and the orbital plane are aligned while the second galaxy is inclined by $\theta = 30^\circ$ with respect to the orbital plane. We evolve all simulations for 5 Gyr, such that the remnant galaxies are relaxed and do not show any obvious signs of a recent merger event.

¹ At this initial distance the two hot gaseous haloes are already penetrating each other. This, in principle, could reduce the strength of the shock at the boundaries of the haloes during the merger. We explicitly tested this by running a simulation with $d_{\text{start}} = 500$ kpc and found no difference in the temperature and density profiles. This is not surprising because of the very low density of the hot gas in the outer regions ($r > 125$ kpc).

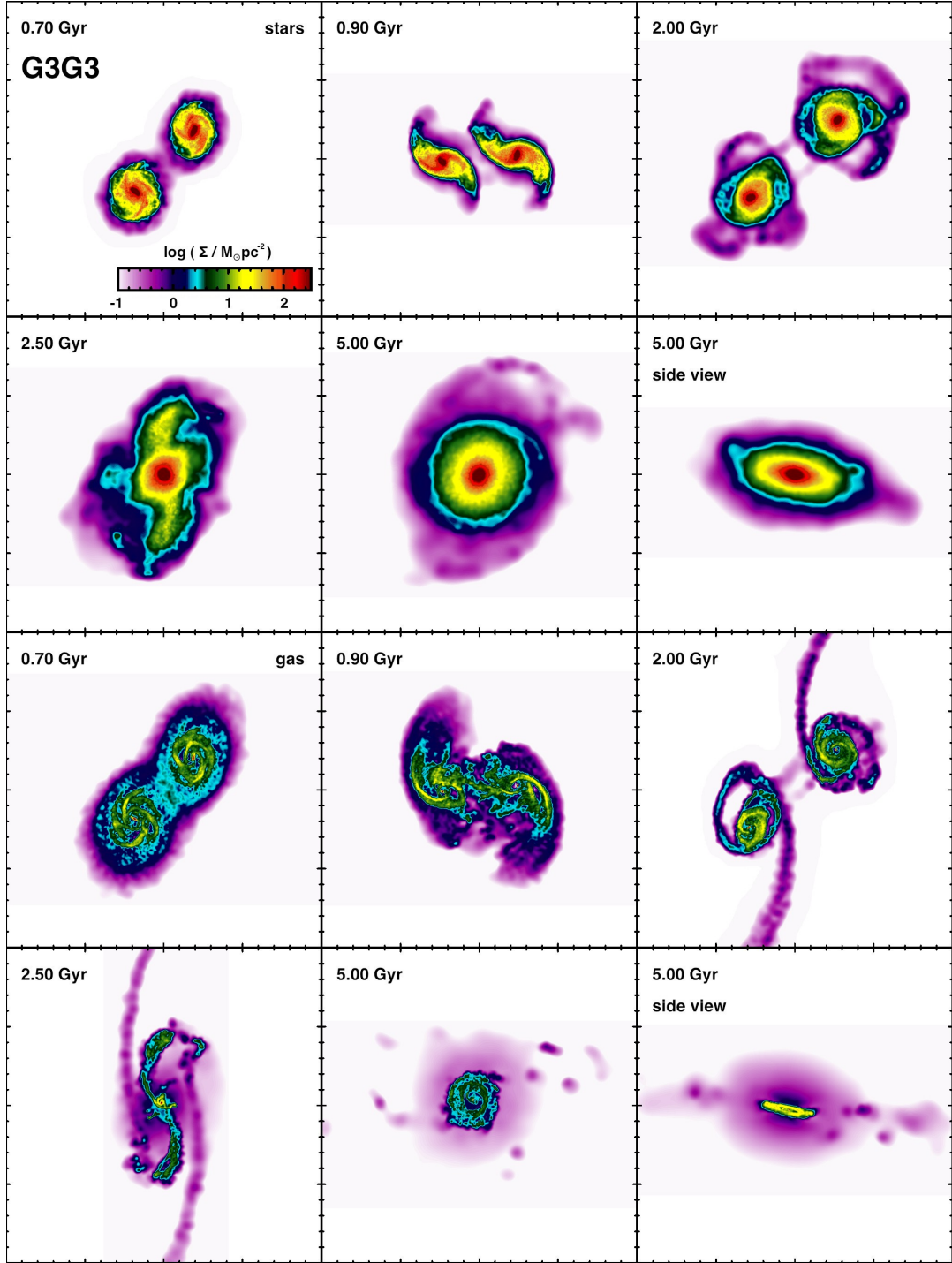


Figure 2. Projected surface density for the stellar component (upper two rows) and the gaseous component (lower two rows) for the merger without hot gaseous haloes and without stellar winds as viewed in the orbital plane. Each panel measures 200 kpc on a side and the time in Gyr is displayed in the upper left corner of each panel. The right-hand panels in the second and bottom columns show a side view of the final merger remnant. The images were created with SPLASH (Price 2007).

3 MAJOR MERGERS

We have simulated the fiducial major merger using four different sets of ingredients: one without stellar winds and without hot gaseous halo (G3G3), one with stellar winds and no gaseous halo (G3G3w), one without winds but with a gaseous halo (G3G3h) and finally one with winds and a

gaseous halo (G3G3wh). The surface density in the orbital plane is shown in Figures 2 (G3G3) and 3 (G3G3wh) for the stellar component (upper panels) and the gaseous component (lower panels).

The discs become tidally distorted as they reach first pericentre ($t \sim 0.8$ Gyr), leading to long tidal tails that drive out loosely bound material while the central regions

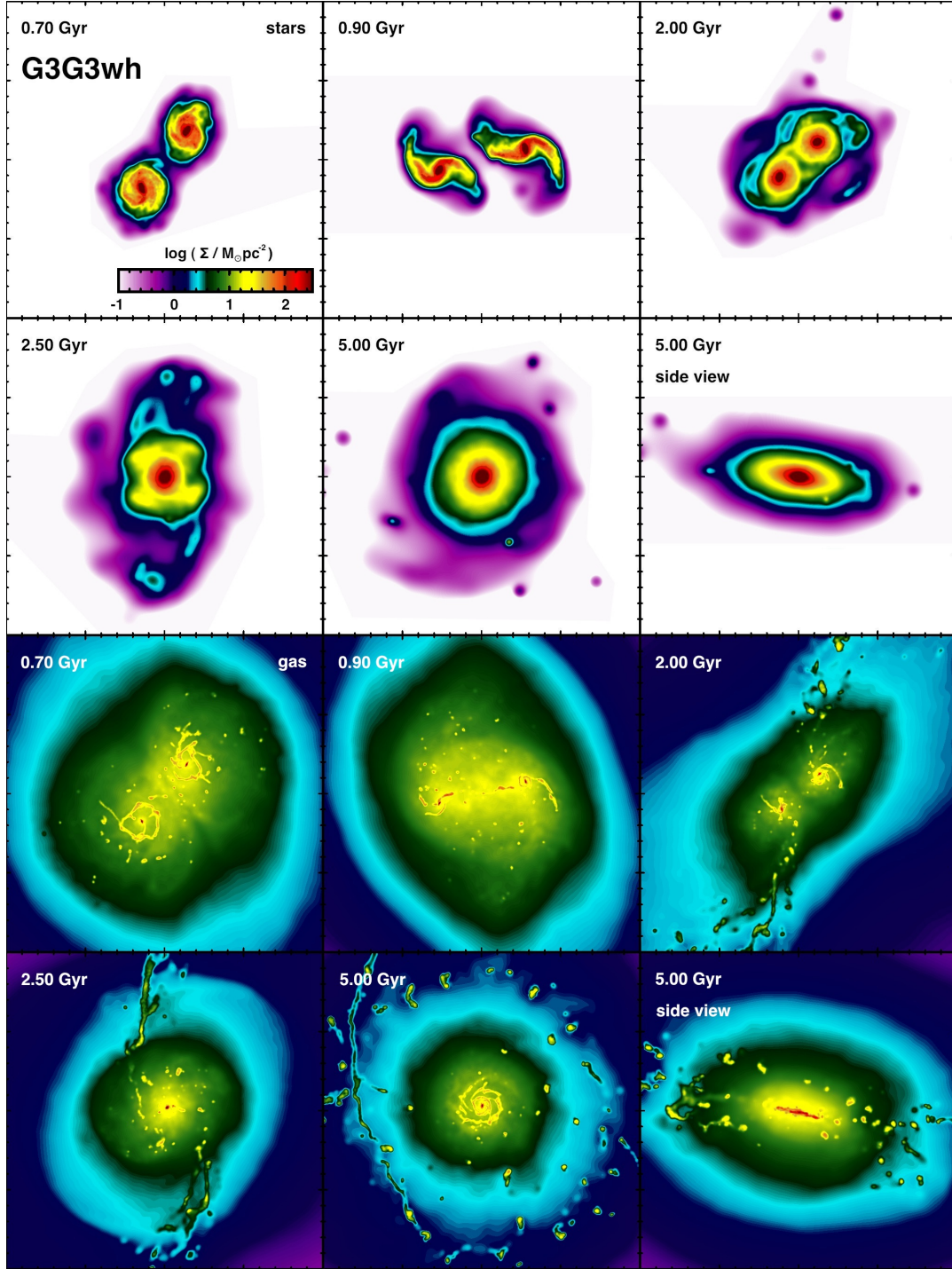


Figure 3. Similar to Figure 2, but for the simulation with stellar winds and hot gaseous haloes.

form bar-like structures. Due to dynamical friction, orbital energy decreases while the spin of the haloes increase, which results in an almost radial orbit after the first encounter. During the second encounter ($t \sim 2.3$ Gyr), both discs are destroyed and the remnant is a spheroidal-looking object. Due to shocks, some of the kinetic energy of the gas is transformed to thermal energy and then radiated away, resulting in an offset between the stellar and the gaseous components. This drags the gas into the dense central regions where the

cooling time is very short, leading to a starburst. In the G3G3 run, heated low-density gas expands from the central region and forms a (low mass) hot gaseous halo after the merger (cf. Cox et al. 2004). Gas from this halo cools again and accretes onto the orbital plane where it forms a cold gaseous disc, subsequently forming a nuclear stellar disc. The G3G3wh run is similar, however, due to the additional potential of the hot gas material, the galaxies merge slightly earlier (~ 150 Myr). The stellar remnant is more flattened

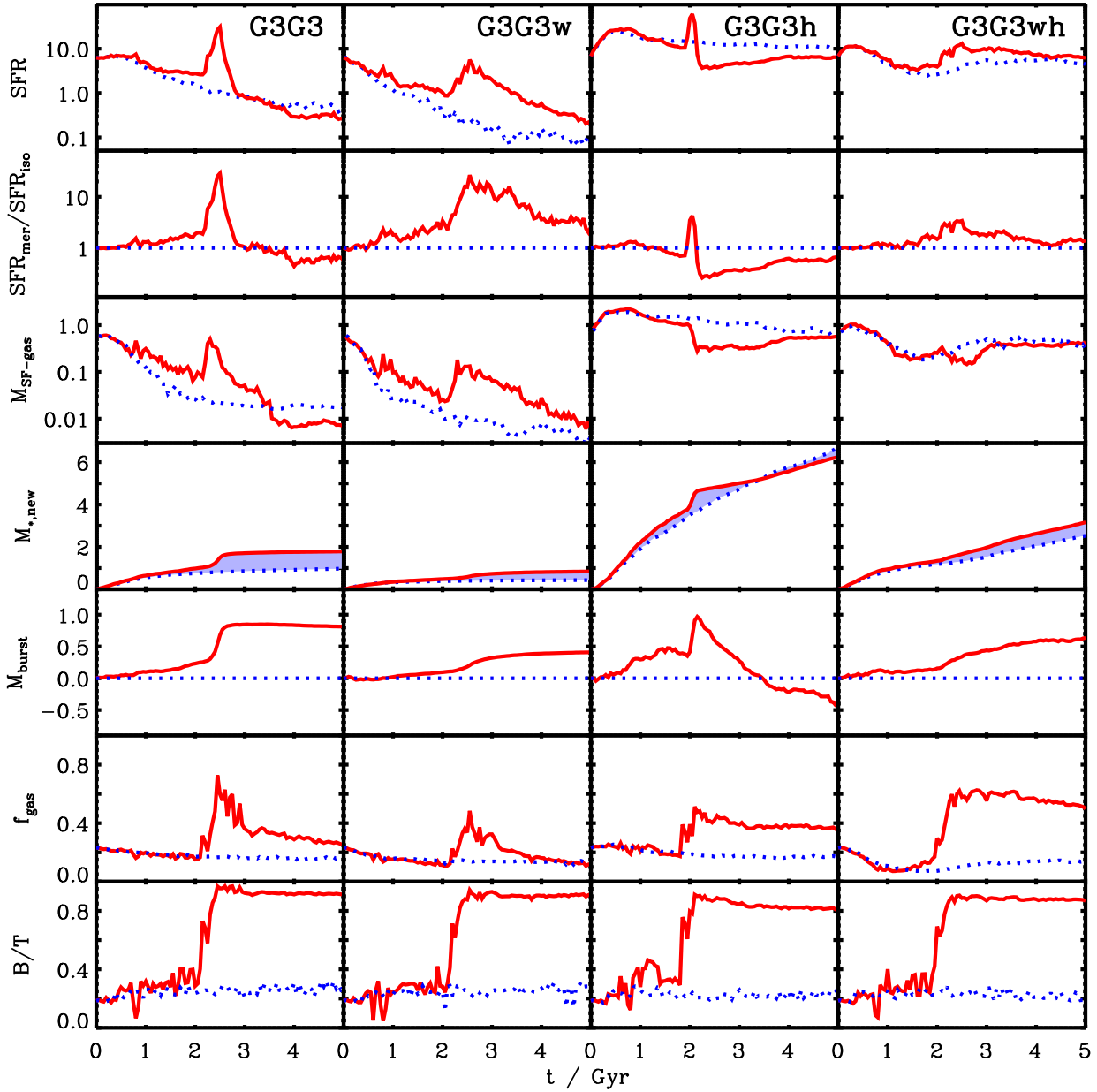


Figure 4. The rows from top to bottom show the total SFR, SFR normalized by the SFR of both isolated galaxies, the mass of dense star-forming gas available, the new stellar mass formed during the simulation, the burst mass, the gas fraction in the disc and the bulge-to-total ratio for the fiducial simulations G3G3, G3G3w, G3G3h and G3G3wh, from left- to right-hand side. The results for the mergers are shown by the solid red lines and for the combined isolated galaxies by the dotted blue lines. All SFRs are given in $M_{\odot} \text{ yr}^{-1}$ and all masses in $10^{10} M_{\odot}$.

than in the G3G3 run. In addition, after the merger there is still a large reservoir of hot gas left in the halo which has received most of the orbital angular momentum. This massive hot halo can reform a much more prominent cold gaseous disc after the merger which is thinner than in the G3G3 run. In both simulations we find several tidal condensations which form from loosely bound tidal material and consist of gas and new stars.

3.1 Star formation

In this and the following section we study the effects of stellar winds and the hot gaseous halo on the SFRs and the efficiency of the starburst. For this we compare the SFRs and the new stellar mass that forms during the simulations between the four merger simulations and for the progenitor galaxies evolved in isolation. We investigate the effect of including stellar winds but no hot halo, a hot halo but no winds, and both winds and a hot halo.

mergers is shown in the first row of Figure 4. The simulation without stellar winds and no gaseous halo (G3G3) agrees very well with the results of Cox et al. (2008): The SFR of the merger (solid line) is clearly enhanced compared to the isolated runs (dotted line). The maximum SFR during the merger ($\sim 30M_{\odot} \text{ yr}^{-1}$) is 30 times larger than the summed SFR of the isolated discs ($\sim 0.5M_{\odot} \text{ yr}^{-1}$), as shown in the second row of Figure 4. The starburst starts shortly before the final coalescence and after the merger, the SFR quickly drops ($\sim 500 \text{ Myr}$) to the value of two isolated discs. We find that in both cases the SFR after 3 Gyr ($< 1M_{\odot} \text{ yr}^{-1}$) is very low compared to the SFR at the beginning of the simulation ($\sim 6M_{\odot} \text{ yr}^{-1}$). This is due to the limited amount of remaining cold gas, which has no source of refuelling. We show the amount of cold star forming gas (i.e. cold gas which also fulfills the density criterion $\rho > \rho_{th}$) in the third row of Figure 4. The amount of dense star-forming gas strongly increases just before the burst, due to the torques driving gas into the nucleus. This star-forming gas reservoir is largely consumed in the burst.

The SFR in the simulation with stellar winds included (G3G3w) drops much more rapidly for the isolated galaxies, as cold gas is expelled from the disc by the winds. After $\sim 3 \text{ Gyr}$ the SFR has dropped by a factor of a hundred. During the merger we also find a starburst, with an enhanced SFR ($\sim 6M_{\odot} \text{ yr}^{-1}$) that is ~ 30 times larger than the summed SFR of the isolated discs ($\sim 0.1M_{\odot} \text{ yr}^{-1}$). With respect to the simulation with no winds, the absolute value of the SFR during the starburst is five times lower. The duration of the starburst is also significantly increased with respect to the windless case. This result was already demonstrated by Cox et al. (2006c), although using a different implementation of stellar feedback. The SFR in the merger is always larger than in the isolated case and equals that of the isolated discs only at the end of the simulation. The amount of dense star-forming gas is lower than in the no wind case during the burst. After the burst, however, there is as much star-forming gas available as in the G3G3 run, leading to a similar SFR. The reason for the longer duration of the starburst is that during the starburst, the wind prevents some of the gas from reaching the dense nucleus of the galaxy. This material is then located in a halo around the galaxy and can subsequently cool and accrete onto the disc, leading to a higher SFR.

In the run without winds, but with a hot gaseous halo (G3G3h), the SFR for the isolated galaxy stays relatively constant during the simulation ($\sim 6M_{\odot} \text{ yr}^{-1}$ per galaxy), as the cold gas in the disc is constantly refuelled through cooling from the halo. The starburst in the merger has an enhanced SFR of $\sim 60M_{\odot} \text{ yr}^{-1}$, which is a factor of five times larger than the summed SFR of the isolated discs. However, after the burst the SFR drops to a value that is lower with respect to the isolated case ($\sim 5M_{\odot} \text{ yr}^{-1}$). The reason for this is the lower amount of star-forming gas available after the burst. This means that the cold gas at the centre of the galaxy which is compressed and quickly used up during the burst, is not immediately replenished, indicating that there is a process that hinders the accreting gas from becoming dense and forming stars.

Finally, the SFR for the isolated galaxies in the simulation including winds and a gaseous halo (G3G3wh) is also relatively constant ($\sim 2M_{\odot} \text{ yr}^{-1}$ per galaxy), but lower

than in the G3G3h case due to the stellar winds which remove dense gas from the centre. Although in the merger case there is clearly an enhanced SFR, the peak is not as prominent and the burst is spread over a much larger time interval than in the other cases. With respect to the isolated case, the maximum SFR ($\sim 13M_{\odot} \text{ yr}^{-1}$) is enhanced by only a factor of three. After the burst, the SFR decreases again and reaches a value that is similar to that of the two isolated systems. The reason for this is that the amount of dense star-forming gas is the same in both runs.

In summary we can point out two major effects: (1) In simulations with stellar winds, the starburst is spread over a much larger time interval than in the windless case. This is due to the removal of cold gas from the dense star-forming region in the centre. This material is ejected into a halo around the galaxy and can then cool and accrete back to the centre which results in an enhanced SFR. (2) In simulations that include a hot gaseous halo the enhancement of the SFR in a merger with respect to isolated galaxies is much smaller than in systems that do not include a gaseous halo. The reason is the continuous accretion of cold gas from the halo and the resulting higher SFR in the isolated discs. In simulations without this accretion, most of the gas is already used up by the time of the merger and the rest is then quickly converted into stars during the burst resulting in a high SFR. Isolated galaxies, however, have a very low SFR at the corresponding time, which results in a large difference between merging and isolated galaxies. If the gaseous halo is taken into account, the isolated galaxies also have a considerable SFR, such that the difference between the enhanced SFR during mergers and isolated systems is no longer as large.

3.2 Starburst efficiency

In order to quantify the merger-driven star formation it is common to focus on quantities based on the overall gas consumption rather than details of the time-dependent star formation history, since the latter depends on the adopted feedback model. Various authors have made use of the ‘burst efficiency’ e which is defined as the fraction of cold gas consumed during the merger minus the fraction of cold gas consumed by the constituent galaxies evolved in isolation (Cox et al. 2008; Somerville et al. 2008b). This definition is then useful to predict the additional mass due to the starburst as a function of initial cold gas mass. An equivalent definition is $e = M_{\text{burst}}/M_{\text{cold}}$, where the ‘burst mass’ $M_{\text{burst}} = M_{*,\text{new}}(\text{merger}) - M_{*,\text{new}}(\text{isolation})$ is the stellar mass that formed due to the merger and M_{cold} is the mass of cold gas in the galaxy before the merger. The two main quantities to determine the burst efficiency are thus burst mass and the cold gas mass. It is important at which time these quantities are defined: the cold gas mass has to be defined just before the final coalescence where the gas will lose angular momentum. The burst mass has to be defined just after the merger, i.e. when the SFR of the merging system is at the same level of the isolated galaxies again, otherwise it depends on the amount of time that has elapsed after the merger.

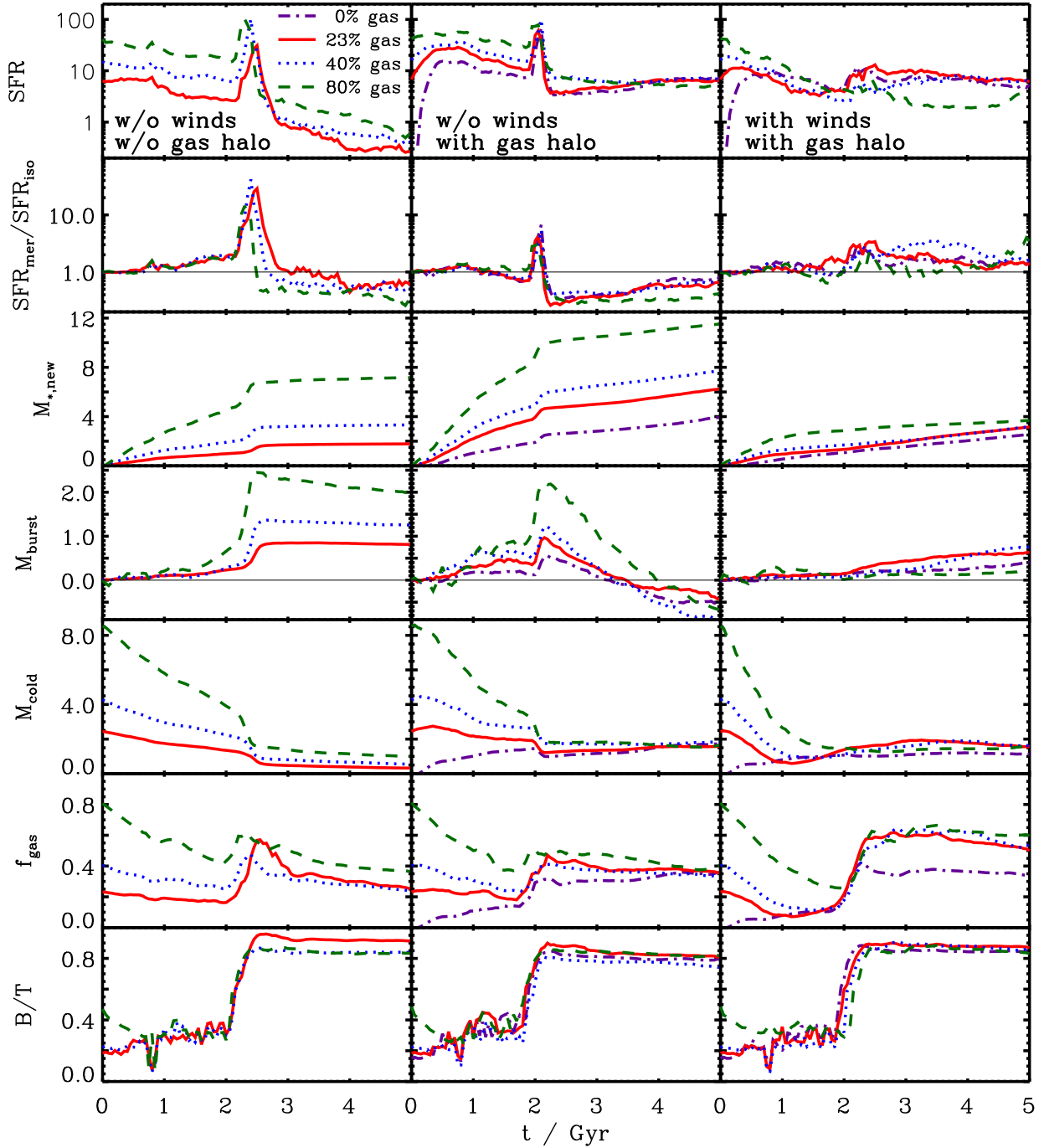


Figure 5. The rows from top to bottom show the SFR, the SFR normalized by the SFR of both isolated galaxies, the new stellar mass formed in the simulation, the burst mass, the cold gas mass, the gas fraction in the disc and the bulge-to-total ratio for the simulations G3G3, G3G3h and G3G3wh from the left- to right-hand side. The various lines represent different initial cold gas fractions in the disc. All SFRs are given in $M_{\odot} \text{ yr}^{-1}$ and all masses in $10^{10} M_{\odot}$.

3.2.1 Dependence on winds and gaseous halo

In the fourth row of Figure 4 we show the new stellar mass formed during the simulation for the isolated (dotted line) and the merger case (solid line). The difference between the isolated and the merger lines is shaded. In the fifth row we plot the burst mass and in the sixth row, we show the cold gas fraction in the disc $f_{\text{gas}} = M_{\text{cold}} / (M_{\text{cold}} + M_{*,\text{disc}})$.

The new stellar mass formed in the simulation G3G3 is enhanced during the starburst, such that the burst mass is $M_{\text{burst}} = 0.84 \times 10^{10} M_{\odot}$. With a cold gas mass just before the burst of $M_{\text{cold}} = 1.25 \times 10^{10} M_{\odot}$ (for both galaxies) this results in a starburst efficiency of $e = 0.68$. Due to the stellar winds, the starburst in the G3G3w case is less efficient: it has a burst mass of $M_{\text{burst}} = 0.4 \times 10^{10} M_{\odot}$ and a cold gas mass

before the burst of $M_{\text{cold}} = 0.9 \times 10^{10} M_{\odot}$ which results in an efficiency of $e = 0.45$. This shows that any parametrization of the starburst efficiency depends on the stellar wind model and its parameters.

In the simulation with a gaseous halo and no winds the mass of the merging system also increases during the burst with respect to the isolated systems. It has a burst mass of $M_{\text{burst}} = 0.97 \times 10^{10} M_{\odot}$ and a cold gas mass before the burst of $M_{\text{cold}} = 1.92 \times 10^{10} M_{\odot}$ resulting in an efficiency of $e = 0.51$. The presence of the hot gaseous halo thus reduces the efficiency of SF, although the absolute SFR is larger in this case. In addition, as the SFR of the merger remnant is lower than that of the isolated systems after the burst, the summed stellar mass of the isolated galaxies increases faster, such that both simulations have the same stellar mass at $t \sim 3.5$ Gyr. At the end of the simulations, the summed stellar mass in the isolated galaxies is larger than that of the merger remnant. The SFR after the starburst is lower than that of the isolated systems, since the amount of dense star-forming gas available is a factor of ~ 4 lower. The initial cold gaseous disc is consumed during the starburst, so that the SFR after the burst depends only on the amount of gas that can be accreted into the dense nucleus. This means that the accretion is more effective in the isolated case than after the merger.

In order to explain what prevents the gas from cooling and becoming dense enough to form stars, we compare the specific angular momentum and the temperature of the hot gaseous halo of the merger remnant and the isolated system at $t \sim 2.5$ Gyr. The specific angular momentum of the gaseous halo in the merger remnant is 25% higher than that of the isolated system, leading to larger centrifugal barrier. As we showed in section 2.2.2, a larger angular momentum decreases the accretion rate and the amount of gas that can reach high enough densities to form stars. While in the isolated case the specific angular momentum stays constant throughout the simulation, in the merger run the hot gas acquires angular momentum from the merger orbit. For our prograde, almost coplanar orbit this results in a larger specific angular momentum after the merger is complete, leading to less dense cold gas available at the centre and thus to a lower SFR.

There is also a second effect that leads to a lower SFR after the merger. When the two gaseous haloes collide, shocks occur and heat the gas, transferring orbital energy to thermal energy. At $t \sim 2.5$ Gyr, just after the starburst, the temperature of the halo gas is $\sim 70\%$ higher than in the isolated run. This leads to a cooling time which is $\sim 35\%$ longer, so that the hot gas in the halo needs more time to cool and accrete onto the disc. This further reduces the accretion rate and thus the amount of cold gas that is available to form stars.

This shows that if the hot gaseous halo is considered in merger simulations, it is possible (depending on orbit, gaseous halo mass, etc.) that isolated systems may have a higher SFR than merging systems, leading to larger stellar masses in systems that have evolved in isolation. This is a serious challenge for the simple recipe that is widely used in semi-analytic models, in which a merger leads to enhanced star formation and therefore to remnants that are more massive than the sum of the constituent galaxies evolved in isolation.

In the simulation with a gaseous halo and stellar winds the mass of the merging system is increased during the burst with respect to the isolated systems. The burst mass is $M_{\text{burst}} = 0.64 \times 10^{10} M_{\odot}$ and with a cold gas mass before the burst of $M_{\text{cold}} = 1.45 \times 10^{10} M_{\odot}$ the efficiency is $e = 0.44$. This value is slightly smaller than that for the case with winds but no gaseous halo, so the presence of the halo reduces the efficiency also in the case with winds. After the burst, the SFR of the merger remnant is still higher than that of the isolated systems and reaches a similar value at the end of the simulation, such that the stellar mass of the merger remnant is larger than the summed mass of the isolated galaxies. In the isolated runs the winds subsequently remove small amounts of cold gas from the dense nucleus, so that the overall SFR is lower than in the case without winds. This material is redistributed into the hot gaseous halo and accretes back onto the disc along with the other cooling gas from the hot halo. In the merger run, a lot of material is removed from the centre during the burst (since the wind rate is proportional to the SFR) in a short time interval, such that suddenly there is a lot of extra material in the hot gaseous halo. This denser and more massive halo is then able to cool more rapidly, leading to more cold dense gas and thus to a higher SFR than in the isolated case. This shows that if stellar winds are included, more stellar mass may be formed in mergers than in isolated galaxies.

Another effect worth noting is that the stellar mass formed during the simulations with a gaseous halo is much larger than in the runs without it. The final mass of the new stars in the G3G3h (G3G3wh) run is a factor of 3.5 (3.7) times larger than the mass in the G3G3 (G3G3w) run, which shows that the gaseous halo is very important to obtain galaxies with realistic masses. In both of the runs with the gaseous halo, all of the initial cold gas in the disc has been consumed by the end of the simulation, while in the other two runs some of the initial cold gas is still left. This left-over gas does not reach densities that are high enough to form stars. If the gaseous halo is present, however, the constant accretion replenishes the gas disc and ensures that the gas reaches densities high enough to form stars.

3.2.2 Dependence on gas fraction

Up to now we have studied mergers with just one fixed initial gas fraction in the disc (23%). In the following section we study how our results depend on the initial progenitor gas fraction. It has been shown by Hopkins et al. (2009a) that the dominant process that removes angular momentum from the gas during a merger is the lag between the stellar bar and the gaseous bar. In very gas rich systems, the stellar mass density is low and the stellar bar is weak or absent. In this case, as shown by Robertson et al. (2006a) and Hopkins et al. (2009a), even major mergers may produce little enhancement in star formation activity and may result in a disc-dominated remnant. Thus, based on merger simulations with no winds and no hot halo, we expect the star formation efficiency in the burst and the remnant morphology to scale with the initial gas fraction in the progenitors. For this study we use our fiducial models, and keep the total mass of the disc fixed but modify the gas content in the disc to 0%, 23%, 40% and 80%. All other parameters remain unchanged from the fiducial values.

Table 3. Burst efficiency for different gas fractions.

Run	$f_{\text{g,init}}^a$	$f_{\text{g,burst}}^b$	M_{gas}^c	M_{burst}^d	e^e
G3G3	0.23	0.16	1.253	0.849	0.678
G3G3f4	0.40	0.25	2.119	1.365	0.644
G3G3f8	0.80	0.41	3.809	2.448	0.643
G3G3hf0	0.00	0.14	1.371	0.553	0.403
G3G3h	0.23	0.18	1.920	0.968	0.504
G3G3hf4	0.40	0.24	2.640	1.218	0.461
G3G3hf8	0.80	0.38	3.580	2.220	0.620
G3G3whf0	0.00	0.11	1.048	0.400	0.382
G3G3wh	0.23	0.11	1.446	0.636	0.440
G3G3whf4	0.40	0.11	1.287	0.672	0.522
G3G3whf8	0.80	0.26	1.405	0.224	0.159

^a gas fraction in the initial disc^b gas fraction in the disc just before the starburst^c cold gas mass just before the starburst in $10^{10} M_{\odot}$ ^d burst mass just after the starburst in $10^{10} M_{\odot}$ ^e starburst efficiency

The results are plotted in Figure 5 for the simulations G3G3, G3G3h and G3G3wh from left- to right-hand side. From top to bottom the SFR, the SFR normalized by the SFR of both isolated galaxies, the new stellar mass formed in the simulation the burst mass, the cold gas mass, the gas fraction in the disc and the bulge-to-total ratio are shown as a function of time. In order to compute the burst efficiency, we use the cold gas mass and gas fraction just before the starburst, and the burst mass just after it. The resulting quantities are given in Table 3.

For the case without winds and gaseous halo (G3G3) we find that the starburst efficiency decreases slightly with increasing gas fraction. This means that if more gas is available in the disc, it is harder to convert all of the gas into stars during the burst. If a hot gaseous halo is included, however, the starburst becomes more efficient with increasing gas fraction. In order to explain this it is important to state that the efficiency mainly depends on the amount of cold gas available for the starburst. This material is of course not the total mass of cold gas in the simulation, but only the cold gas in the nucleus, where the burst occurs. Thus the efficiency is a strong function of the spatial distribution of the cold gas.

In the G3G3 series, the fraction of the cold gas at the centre (< 5 kpc) is very similar in all runs which means that the amount of gas available for the starburst scales with the total gas mass. In the G3G3h series, however, we find that the fraction of the cold gas at the centre is higher for the runs with a large initial gas fraction. For these runs, most of the dense initial gas disc is still present when the burst occurs and can participate in it, while for runs with a lower gas fraction, a large fraction of the initial gas disc has already been consumed, so that much of the cold gas is material that has been accreted from the halo. This accreted material is distributed in a more extended configuration and cannot contribute to the starburst, as it is far from the nucleus. The result is that systems with a high initial gas fraction have a

larger amount of material that can participate in the burst than systems with a low initial gas fraction, such that they are more efficient. The efficiency of runs with gaseous haloes, where some of the cold gas was accreted from the halo and is not centrally concentrated, are always lower than for the corresponding runs without gaseous haloes, where all the cold gas resides in the more centrally concentrated initial disc.

In the simulations with stellar winds there are three runs with the same gas fraction just before the merger (11%), but with a different burst efficiency which increases with increasing initial cold gas mass. The explanation is similar to the case with no winds: runs with a larger initial cold gas mass retain a larger amount of the initial dense disc, while in runs with a lower initial gas mass, there is a larger fraction of gas that has accreted from the halo and is not as centrally concentrated. Thus the mass of the gas that can participate in the burst is larger in runs with a higher initial gas fraction, resulting in a higher burst efficiency.

The run with 80% initial gas fraction has a lower efficiency than the other G3G3wh runs, as the burst mass is very low. The main question is why the run with the high initial gas fraction has a decreased efficiency with respect to lower initial gas fractions, while for the simulations without winds the runs with a higher initial gas fraction have a larger efficiency. To answer this, we measure the mass of the stellar disc just before the burst: in the G3G3h series the disc mass is very similar for all runs, as most of the initial gas disc has been transformed into the stellar disc. In the G3G3wh series, however, the stellar mass of the disc is very low for high initial gas fractions, since the stellar winds remove a lot of gas from the disc and thus lower the SFR. The stellar disc mass of G3G3whf8 is only half the value of the disc in G3G3wh just before the burst. As a consequence the amount of stellar mass available to form a bar which can remove angular momentum from the gas is lower in the G3G3whf8 run, resulting in less material that can be dragged into the centre during the burst. Therefore the burst efficiency is reduced.

Overall, we find that the starburst efficiency depends strongly on the presence of the hot gaseous halo and the stellar winds (and on their parametrization). When both are neglected, the burst efficiency is a weak function of gas fraction and decreases with increasing f_{gas} . Both the gaseous halo and the winds reduce the burst efficiency. When the gaseous halo is included, the efficiency decreases with decreasing gas fraction, as the initial dense disc is replaced by accreted gas from the halo which is spatially much more extended. When stellar winds are also included, the efficiency for systems with a high initial gas fraction is decreased, since the winds prevent the formation of a massive stellar disc before the merger, which is needed to form a stellar bar that can drag the gas to the centre of the burst.

3.3 Morphology of the merger remnant

Having investigated how the SFR changes during the merger, we now focus on the properties of the merger remnant at the end of the simulation. To this end, we decompose the stellar particles into a spheroidal and a disc component using the following method. For every particle, we compute the angular momentum along the spin axis and divide this by the angular momentum the particle would have on a cir-

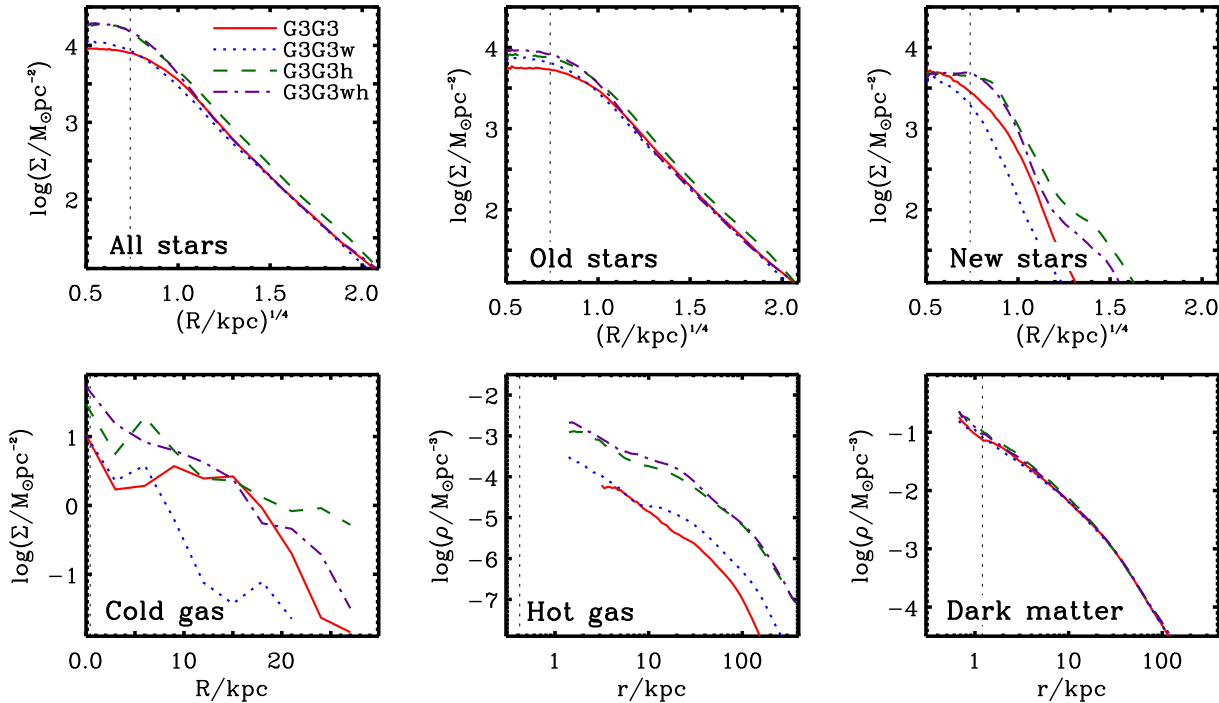


Figure 6. *Upper panels:* Surface density profiles averaged over 100 projections for all, old and new stars from left- to right-hand side. *Lower left panel:* Surface density profiles of the cold gas as seen face-on. *Lower middle panel:* 3d density profiles of the hot gaseous haloes. *Lower right panel:* 3d density profiles of the dark matter halo. The various lines show the different simulations: G3G3 (no winds, no gaseous halo), G3G3w (with winds, no gaseous halo), G3G3h (no winds, with gaseous halo) and G3G3wh (with winds, with gaseous halo). The dotted vertical lines indicate three times the softening length and hence the resolution limit.

cular orbit at the same radius. The spherical component is then distributed around a value of zero, while the disc component is centred at unity, such that the two components can be separated easily (Abadi et al. 2003). In the lower panels of Figure 4, we plot the resulting bulge-to-total ratio $B/T = M_{\text{bulge}}/M_*$ for the four fiducial runs. In all simulations the disc component just after the starburst is almost completely destroyed. In the runs without the gaseous halo, the B/T after the burst is ~ 0.9 and stays at this value until the end of the simulation. If a gaseous halo is included, the B/T after the burst is also ~ 0.9 , but then decreases to ~ 0.8 for G3G3h and ~ 0.85 for G3G3wh. The reason for this is that due to the accretion of gas from the halo, a much larger cold gaseous disc can form after the burst which leads to a much larger stellar disc. Because of the stellar winds in G3G3wh, cold gas is subsequently removed from the disc, leading to a lower mass stellar disc at the end of the simulations and thus to a larger B/T compared to G3G3h. Still, all four remnant systems are still very much bulge dominated.

We also find that the bulge-to-total ratio decreases with increasing initial gas fraction. However, even for $f_{\text{g,init}} = 0.8$ the final value is $B/T = 0.85$, while for the lower $f_{\text{g,init}} = 0.23$ case the final bulge-to-total ratio is only slightly higher: $B/T = 0.9$. This is mainly due to the low SFR after the burst, so that the mass in the new stellar disc that forms after the merger is very low ($M_* = 5 \times 10^9 M_\odot$ for the 80 percent gas case) as can be seen in the third row of Figure 5. The final bulge-to-total ratio in the simulations with a hot gaseous halo is very similar in all runs, independent of the initial cold gas fraction and whether stellar winds

are enabled. The reason for this is that the SFR after the merger does not depend on the initial cold gas mass and distribution, but only on the accretion rate after the merger. As the latter only depends on the mass, temperature and profile of the hot gaseous component, the SFRs are very similar for all runs, as can be seen in the first row of Figure 5. As a result the mass in the new stellar disc that forms after the merger is very similar in all simulations which yields very similar bulge-to-total ratios.

In order to study how the stellar mass is distributed within the merger remnants, we compute the azimuthally averaged surface density profiles for old, new and all stars, where old stars are the stellar particles which were present before the burst (i.e. particles created for the initial conditions and particles formed through SF) and new stars are those stellar particles that formed through SF during and after the burst. The upper panels of Figure 6 show the results for the four fiducial runs. The profiles for all stars at scales beyond ~ 1 kpc are very similar for all remnants following the observed $r^{1/4}$ profile. The slope is identical for all runs and only the normalization of G3G3h is higher than that of the other runs, as the stellar mass before the burst was already much larger. This can also be concluded from the profiles of the old stars: as the mass of the old stellar component is very similar for all runs, except for G3G3h, their final profiles have the same normalization. The contribution from new stars at these scales is very small for all runs. The surface density profiles in the outer parts are in agreement with profiles obtained by dissipationless simulations (Naab

& Trujillo 2006), which shows that the gas physics plays a negligible role far from the centre.

At small scales ($R \lesssim 1$ kpc) the stellar surface density of the systems with a gaseous halo is higher compared to the other two simulations. Not only is the surface density of the new stars larger, which can be simply explained by the more massive stellar discs in the centre, but also the surface density of the old stars is higher. The reason for this is the central concentration of new stars, which steepens the potential well and draws the old stars into the centre. We note that, up to the resolution limit of ~ 3 times the softening length (e.g. Klypin et al. 2001), the surface density profiles of the runs with a gaseous halo follow the observed $r^{1/4}$ profile and show neither a cusp nor a core. Our simulations are in agreement with previous studies (Kormendy et al. 2009; Hopkins et al. 2008, 2009b,c), who find that including a large fraction of cold gas in merger simulations leads to a steeper slope in the centre ('extra light') and to a lower Sérsic index that is distinct from the main body. However, in contrast to simulations that do not include a hot gaseous halo we find that large amounts of cold gas are not required in the progenitor discs, as gas can be accreted from the halo after the merger resulting in the formation of a dense stellar core.

In the lower left panel of Figure 6 we show the face-on density profiles of the cold gas component. In the G3G3 run, the profile of the gas disc is very flat up to 15 kpc but has a very dense central concentration ($R < 2$ kpc). When stellar winds are enabled much of the cold gas is ejected from the disc, leading to a very low surface density, except for a dense centre. For the runs with a gaseous halo, a lot of gas is accreted from the halo and settles into an exponential disc. The scale length of this disc is lowered if winds are included. This can be explained by the lower SFR resulting in a lower stellar mass at the end of the simulation and the fact that low mass galaxies have a smaller scale length than massive galaxies (Barden et al. 2005).

The lower middle and right panels show the 3d density profiles for the hot gas and dark matter, respectively. The density of the hot gas for runs with an initial gaseous halo are almost identical. Only at scales of 5–50 kpc, the density in the G3G3wh run is a little higher, as gas that is heated and ejected from the disc by the winds is added to the hot gas reservoir and accumulated at these scales. For the runs without an initial gaseous halo, we see that a hot halo forms due to the merger. In the G3G3 run this hot halo forms from gas that is shock-heated during the merger and has expanded into the halo (Cox et al. 2006a). In the G3G3w run, the density of this halo is enhanced by the material ejected by the wind. The dark matter profile is nearly indistinguishable for all four runs: an NFW-like profile modified by the baryonic contraction, with a slightly higher central density for systems with a gaseous halo.

3.3.1 Kinematic properties

Having determined the mass distribution of the merger remnants, we now study their kinematic properties, i.e. how much the remnants are supported by rotation. The elliptical shape of a rotating galaxy can be understood as a result of flattening induced by rotation. The elliptical structure of a non-rotating galaxy, however, must be supported by something other than rotation, most likely by velocity anisotropy.

This trend can be visualized by plotting the rotation velocity v_{maj} divided by the central velocity dispersion σ against the ellipticity ϵ . In this anisotropy diagram v_{maj}/σ is a measure of the rotational support and ϵ indicates the deviation from a circle.

An analytic relation between the intrinsic ellipticity ϵ_{intr} and $(v_{\text{maj}}/\sigma)_{\text{edge}}$ for edge-on projections has been derived by Binney (2005). For a given anisotropy of the system δ one can plot a distinct line in the ϵ - v_{maj}/σ plane. For a fixed amount of rotation, the intrinsic ellipticity is lower in isotropic systems and larger in anisotropic systems. For an observed galaxy at a given inclination, the observed ellipticity and $(v_{\text{maj}}/\sigma)_{\text{obs}}$ can be computed from the intrinsic ellipticity and $(v_{\text{maj}}/\sigma)_{\text{edge}}$ (see Binney & Tremaine 1987, §4.3). If viewed face on ($\epsilon = 0$), no rotation can be observed, while edge-on ($\epsilon = \epsilon_{\text{intr}}$) the observed rotation velocity is maximal.

In order to compute the three quantities ϵ , v_{maj} and σ , for our simulated remnants, we follow Cox et al. (2006b) and refer to this work for details. Here, we give a brief outline of the procedure. First, the stellar particles are projected onto a plane as if observed from a random viewing angle. Then we determine the isodensity contour that encloses half of the stellar mass and fit an ellipse to it. The ellipticity is computed as $\epsilon = 1 - b/a$, where a is semi-major and b the semi-minor axis of the ellipse. A slit is then placed along the major axis with a length of $3a$ and a width of $a/4$. This slit is divided into 26 bins, lengthwise, and the line-of-sight velocity distribution is computed for each bin. Then the mean velocity and the velocity dispersion are extracted from each bin. Finally, v_{maj} is defined as the average absolute value of the maximum and minimum mean velocity along the slit and σ as the average dispersion of the bins within $a/2$.

Figure 7 shows the resulting anisotropy diagram for our fiducial merger remnants. The left panel compares the four runs and shows v_{maj}/σ vs. ϵ for 1000 random projections for each remnant. In each panel we plot the location of edge-on oblate galaxies with different anisotropy δ as given by the analytic recipe (solid lines). For each simulated remnant we compute the intrinsic ellipticity and the corresponding $(v_{\text{maj}}/\sigma)_{\text{edge}}$ indicated by the black symbol. The anisotropy of the remnant can be obtained by finding the line on which the symbol lies. The dashed lines indicate projections with different inclinations for the analytic galaxy model and trace the projections of the simulations very well.

The merger simulation with no winds and no gaseous halo leads to a remnant which is only slowly rotating, with a maximum rotation velocity of $\sim 50 \text{ km s}^{-1}$ and a maximum v_{maj}/σ of ~ 0.25 . This means that the G3G3 remnant is mostly supported by velocity dispersion and not by rotation. The intrinsic ellipticity and the anisotropy parameter are relatively large ($\epsilon_{\text{intr}} = 0.49$ and $\delta = 0.4$). The main contribution to the rotation comes from the re-formed stellar disc at the centre of the remnant. This explains why the rotational support increases with increasing ellipticity, as when viewed edge-on both ϵ and the observed rotation velocity of the disc are maximal. When viewed face-on, one cannot observe any rotation of the disc. For the simulation with winds, the stellar disc is much smaller, leading to an even smaller disc contribution to the rotation. This results in lower values for v_{maj}/σ and an anisotropy diagram which is similar to that of a remnant in a dissipationless simula-

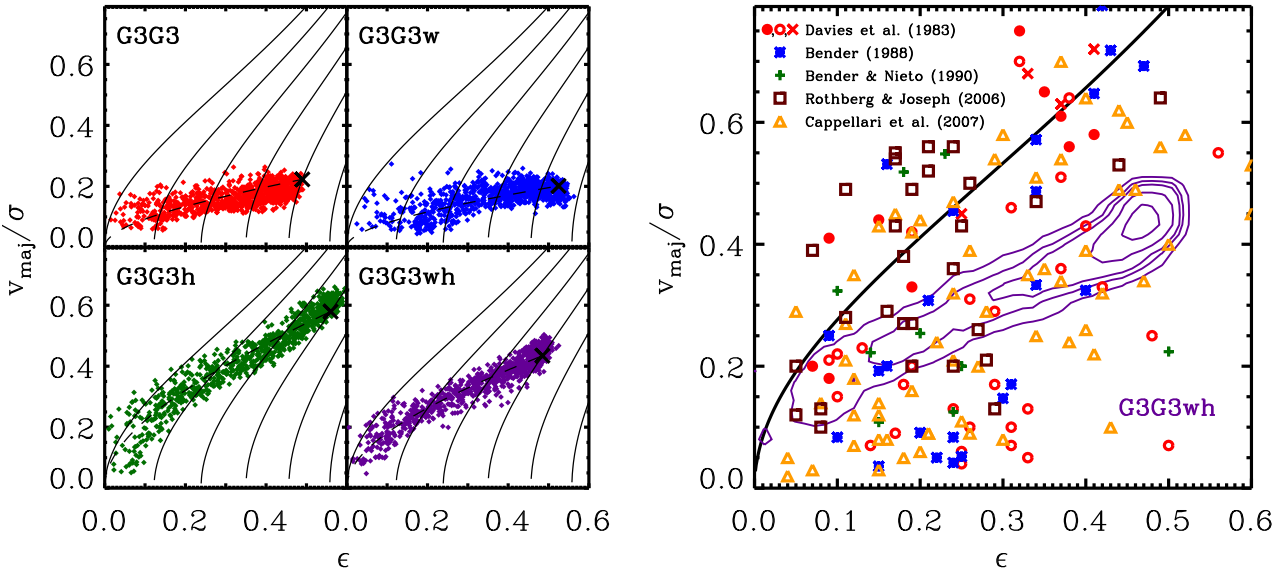


Figure 7. Anisotropy diagram: v_{maj}/σ vs. ellipticity, where v_{maj} is the maximum rotation velocity measured in a slit along the major axis and σ is the velocity dispersion averaged within half of the half-mass radius. The ellipticity is measured at the half mass isophote. *Left panel:* Comparison between the four fiducial simulations, where every point corresponds to one projection. The solid lines are the locations expected for edge-on oblate galaxies with different anisotropy $\delta = 0, 0.1, \dots, 0.5$. The black symbols indicate the intrinsic ellipticities. The dashed lines give the projections for different inclinations. *Right panel:* Comparison between the simulation with winds and a gaseous halo and data from observed elliptical galaxies. The contours indicate the 10%, 30%, 50%, 70% and 90% probability of finding a merger remnant in the enclosed area. The solid line plots edge-on models with $\delta = 0$.

tion. The intrinsic ellipticity and the anisotropy parameter are even larger ($\epsilon_{\text{intr}} = 0.53$ and $\delta = 0.45$) than in the simulation without winds.

When a gaseous halo is included, v_{maj}/σ increases strongly with increasing ϵ , which can be explained by the more massive stellar disc that forms after the merger. When viewed edge-on, the stellar disc dominates within the slit in which the velocity is measured and thus leads to a higher mean rotation velocity. The remnant has an intrinsic ellipticity of $\epsilon_{\text{intr}} = 0.56$ and corresponds to a galaxy model with an anisotropy parameter of $\delta = 0.3$. This indicates that the elliptical shape of the remnant at the half-mass isophote ($R \sim 5$ kpc) is partly due to rotation. If stellar winds are included in the simulation, the mass of the stellar disc is lower, leading to a smaller contribution to the velocity profiles compared to the run with no winds. This also results in lower values of v_{maj}/σ , however, the remnant is still partly supported by rotation. It has an intrinsic ellipticity of $\epsilon_{\text{intr}} = 0.49$ and an anisotropy parameter of $\delta = 0.3$. This shows that in the presence of a cooling hot gas halo, rotationally supported systems can be created even for moderate initial cold gas fractions, and for orbits which lead to systems that are supported only by velocity dispersion when the gaseous halo is not included.

The right panel of Figure 7 compares the remnant of the G3G3wh run to data from several observational samples (Davies et al. 1983; Bender 1988; Bender & Nieto 1990; Rothberg & Joseph 2006; Cappellari et al. 2007). The contours give the 10%, 30%, 50%, 70% and 90% probability of finding a G3G3wh merger remnant in the enclosed area. It is apparent that the simulated remnant agrees well with the observations. There are two main possibilities that can change the area of $v_{\text{maj}}/\sigma - \epsilon$ space that the simulated rem-

nant can cover. First, by decreasing (increasing) the wind efficiency, we can achieve larger (smaller) values of v_{maj}/σ for a given ϵ , up to the limit of no winds (G3G3h), thus reproducing the observed remnants with a large rotational support. Second, by lowering the initial mass of the gaseous halo, we can achieve smaller values of v_{maj}/σ for a given ϵ and can thus reproduce the observed remnants with a small rotational support. Note that by employing the universal baryonic fraction in the initial conditions we have used an upper limit for the mass of the gaseous halo. Through feedback, it is possible to decrease the mass of the halo before the merger. See section 3.4 for a discussion.

3.3.2 Isophotal shape

Finally, we study how the shape of the isophotes change when a hot gaseous halo is included in the merger simulations. To this end, we measure the deviations of the isoden-sity contour of a projection to a fitted ellipse. The residuals are expanded in a Fourier series and the Fourier coefficient a_4 is computed. Positive values of a_4 indicate discy isophotes, while negative values indicate boxy isophotes. The results of this analysis are shown in Figure 8, which plots the ellipticity against the shape parameter a_4 (normalized by the semi-major axis and multiplied by a factor of 100) for our fiducial simulations with 1000 projections each. The left panel compares the four runs. The simulations with no winds and no gaseous halo can appear discy or boxy, depending on the viewing angle, with a tendency towards boxy isophotes. If winds are included, the isophotes can still be discy, however, they are more boxy on average. When a gaseous halo is included, the shape of the isophotes is more discy, especially at high ellipticities. If both winds

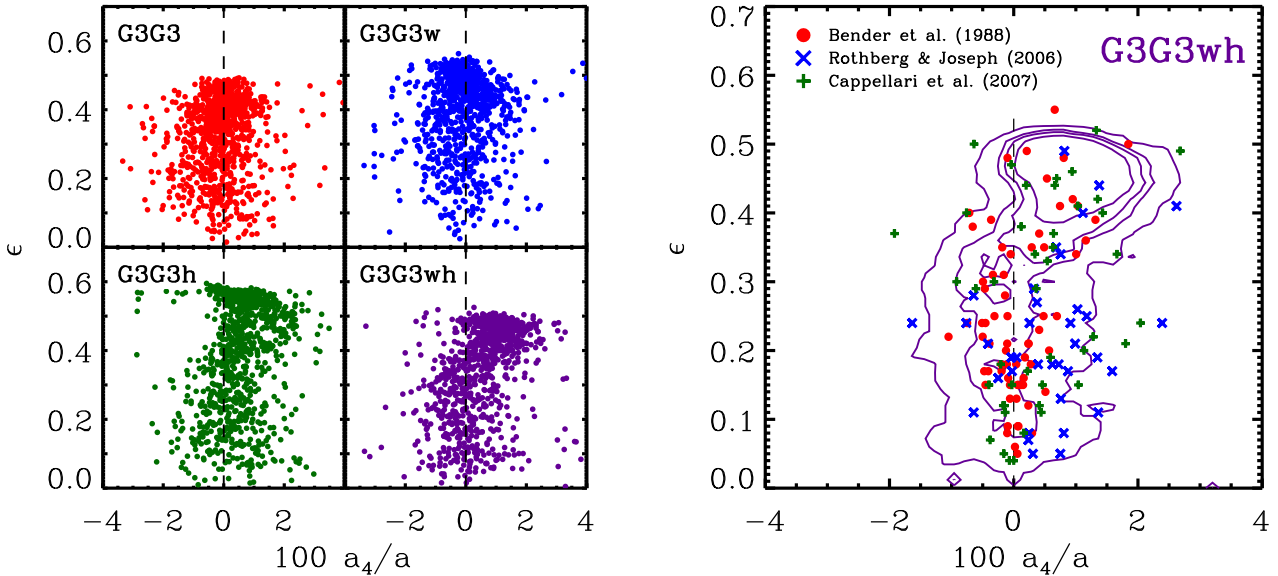


Figure 8. Ellipticity ϵ vs. characteristic shape parameter a_4 , both measured at the half mass isophote. *Left panels:* Comparison between the four fiducial simulations, where every point corresponds to one projection. *Right panel:* Comparison between the simulation with winds and a gaseous halo and data from observed elliptical galaxies. The contours indicate the 10%, 50%, 70% and 90% probability of finding a merger remnant in the enclosed area.

and a gaseous halo are present the isophotal projections are mostly discy. However, at low ellipticities ($\epsilon < 0.3$) the probability for boxy and discy isophotes is equal.

As a result, we find that including a gaseous halo results in more cold gas at the centre, leading to more discy isophotes. This is in agreement with results by Springel (2000), Cox et al. (2006b) and Naab et al. (2006), who find that mergers with gas increase the fraction of discy isophotes. Naab et al. (2006) argue that the reason for the lack of boxy projections in simulations with gas is the different behaviour of minor-axis tube orbits (which are the dominant family around the half-mass radius) in axisymmetric and triaxial potentials. Dissipational mergers lead to more axisymmetric potentials, and in those, minor-axis tubes look less boxy and more discy in all projections. Additionally, the fraction of box orbits and boxlets, which can support a boxy shape, is reduced.

The right panel of Figure 8 compares the remnant of the G3G3wh run to data from observational samples (Bender et al. 1988; Rothberg & Joseph 2006; Cappellari et al. 2007). The contours give the 10%, 50%, 70% and 90% probability of finding a G3G3wh merger remnant in the enclosed area. The simulated merger remnant agrees very well with the isophotal shapes of observed ellipticals. At low ellipticities, there are both discy and boxy projections, with an equal probability. At higher ellipticities ($\epsilon > 0.4$) the chances to find boxy isophotes are very small. These trends are similar to those seen in the observational data.

3.4 Lower initial hot gas mass

In the previous sections we have employed model galaxies with a maximal hot gas halo, i.e. we chose the hot gas mass such that the baryonic fraction within r_{vir} was the universal value. This was done in order to demonstrate the maximum effect this hot gaseous halo can have on the SFR, the star-

burst efficiency and the remnant morphology, in comparison to the case in which the hot gas is neglected. Of course, both cases are the relative extremes, as feedback can decrease the mass of hot gas in the halo before the merger. Therefore we run a merger simulation in which we used only half of the ‘full’ halo mass (G3G3whX) as an intermediate case and compare it to the simulations with the extreme hot gas cases (G3G3w and G3G3wh) in order to check whether the results of the intermediate case fall between the extreme cases. This additional simulation is evolved for 8 Gyr with enabled stellar winds and using the same orbital parameters as in the previous runs.

On the left-hand-side of Figure 9, we show the SFRs during the merger normalized by the SFRs of the respective isolated galaxies and the new stellar mass formed during the simulations. The left, middle and right panels show the runs without a hot gaseous halo, with the ‘full’ hot gas mass and with half of the ‘full’ hot gas mass, respectively. The G3G3whX simulation has a maximum SFR that is enhanced by a factor of ~ 7 with respect to the isolated runs. This value falls just between those of the simulations G3G3w and G3G3wh with an enhancement of ~ 30 and ~ 3 , respectively. The new stellar mass that has formed by $t = 5$ Gyr is $1.3 \times 10^{10} M_{\odot}$ for the G3G3whX runs, while in the runs G3G3w and G3G3wh the stellar mass formed is $0.8 \times 10^{10} M_{\odot}$ and $3.2 \times 10^{10} M_{\odot}$. This shows that the star formation in the run with half of the ‘full’ hot gas mass is an intermediate case between the two extremes.

With a burst mass of $M_{\text{burst}} = 0.22 \times 10^{10} M_{\odot}$ and a cold gas mass before the burst of $M_{\text{cold}} = 0.5 \times 10^{10} M_{\odot}$ the starburst efficiency for the G3G3whX run is $e = 0.44$. This value is very close to the values obtained for the G3G3w and G3G3wh runs, $e = 0.45$ and $e = 0.44$, respectively. This means that in the case with stellar winds, the starburst efficiency does not depend strongly on the hot gaseous halo mass.

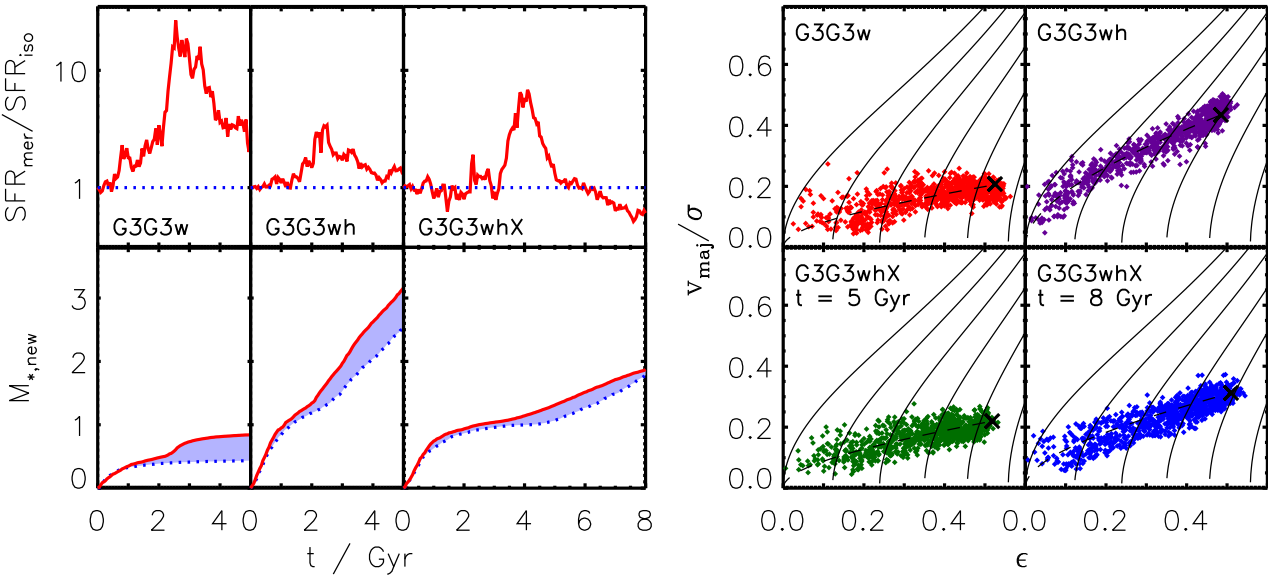


Figure 9. *Left panels:* The two rows show the SFR normalized by the SFR of both isolated galaxies and the new stellar mass formed in the simulation for the simulations G3G3w, G3G3wh and G3G3whX, from left- to right-hand side. The results for the mergers are shown with solid lines and for the combined isolated galaxies by the dotted lines. All masses are in $10^{10} M_{\odot}$. *Right panels:* v_{maj}/σ vs. ellipticity (anisotropy diagrams, cf. Figure 7). The four panels show a comparison between the simulations G3G3w, G3G3wh and G3G3whX at $t = 5$ Gyr and G3G3whX at $t = 8$ Gyr.

On the right-hand side of Figure 9, we compare the kinematic properties of the merger remnants, plotting anisotropy diagrams for the runs G3G3w, G3G3wh and G3G3whX at $t = 5$ Gyr and for G3G3whX at $t = 8$ Gyr. While the simulation including the ‘full’ hot gas mass forms a remnant that is supported by rotation, the simulation with half of the ‘full’ hot gas mass is only slowly rotating after 5 Gyr. However, when evolved to 8 Gyr, the rotational support of the system has increased, although not as much as in the case with the ‘full’ hot gas mass. The reason for this is that in the G3G3whX run, the lower hot gas mass leads to slower cooling and accretion and thus to a lower SFR. Therefore it takes longer to form a prominent stellar disc after the merger, and it is this disc that is responsible for the rotation. As a result we see that the model with half of the ‘full’ hot gas mass can lead to a rotationally supported remnant as well, although it takes longer and the amount of rotation is less than for the model that employs the universal baryonic fraction within r_{vir} .

Haloes in the Universe have baryonic fractions between the extreme cases (universal fraction and no hot gas at all). The actual value will depend on the merger history of a given system, the amount of feedback during its evolution and its environment. We conclude that our results for the extreme cases thus give upper and lower limits for actual galaxies and the results for the simulation with half of the ‘full’ hot gas mass are one possible example within these limits.

4 CONCLUSIONS AND DISCUSSION

We investigated the role of a cooling gaseous halo in merger simulations using the parallel TreeSPH-code GADGET-2. To do this we have extended the initial conditions to include a hot gaseous halo (in addition to a dark matter halo, a stel-

lar bulge and a disc consisting of stars and cold gas). We adopted the observationally motivated β -profile to describe the hot gas and required the halo to be in hydrostatic equilibrium. Furthermore the gaseous halo is rotating around the spin axis of the disc. We have fixed the initial angular momentum of the hot gas by requiring that the specific angular momentum of the gas halo is a multiple α of the specific angular momentum of the dark matter halo and treated α as a free parameter.

Cosmological simulations without cooling, star formation, or feedback show that the spin parameter of hot gas within dark matter haloes is the same as that of the dark matter (van den Bosch et al. 2002), which would correspond to $\alpha = 1$. However, it has been shown that if this hot gas collapses to form a disc while conserving its angular momentum, the disc profiles do not match observations — there is too much low angular momentum material (van den Bosch 2001; Bullock et al. 2001). These results are supported by the results of our simulations: if we allow hot gas with $\alpha = 1$ to cool and form a disc in an isolated halo, we do not reproduce the observed size vs. stellar mass relation for discs (our discs are too small). It has been suggested that winds could preferentially remove low angular momentum material, resulting in a higher average specific angular momentum for the gas relative to the dark matter ($\alpha > 1$). Indeed, recent simulations including stellar driven outflows do show this effect (Governato et al. 2010). However, the results of these simulations are likely sensitive to the details of the “sub-grid” recipes used to model stellar feedback. We therefore adopted an empirical approach in order to constrain the initial value of α for our hot haloes.

This was done by modelling a typical MW-like galaxy at $z = 1$ and letting it evolve in isolation up to $z = 0$ using different values of α . We employed two observational constraints, stellar mass and disc scale length, in order to

determine the correct α . The results for the control simulation without a hot halo disagreed drastically with the observations, which supports the importance of the gaseous halo. Simulations with a low value of α showed both an increase of stellar mass which was too large and scale lengths that were too small compared to observations. Large values of α led to overly large discs and stellar masses that were too low. Only a value of $\alpha \sim 4$ produced stellar masses and scale lengths that were within the observational constraints for MW-like galaxies. This value was then used for all of our simulations with hot haloes.

In order to fix the mass of the gaseous halo we required that the baryonic fraction within the virial radius should be equal to the universal value. We made this choice because we wanted to demonstrate the maximum effects that the hot halo can have in galaxy mergers. Of course, due to feedback processes and stellar winds, the baryonic fraction in galaxies can be lower, leading to a lower mass for the gaseous halo. In the past, several studies have raised the question of whether massive gaseous haloes such as those predicted by galaxy formation models, and adopted in our simulations, violate constraints from X-ray observations. In one such study, Benson et al. (2000) compared X-ray observations of three massive spirals to predictions of simple cooling flow models and found that the model overpredicted the X-ray luminosity by more than an order of magnitude. However, they assumed that the hot gas follows either an isothermal or an NFW profile, which results in very high gas densities in the centre and such results in very high X-ray luminosities.

Current observational measurements on the 0.3-2 keV X-ray luminosity of MW-like systems indicate limits of several $10^{39} \text{ erg s}^{-1}$ (Wang et al. 2003; Strickland et al. 2004; Wang 2005; Tüllmann et al. 2006; Li et al. 2007; Sun et al. 2009; Owen & Warwick 2009). These observational limits have been compared to the X-ray luminosities found in cosmological hydrodynamic simulations by Rasmussen et al. (2009). They found no tension between simulations and observations (for a simulated MW-like galaxy they found 0.3-2 keV X-ray luminosities of $\sim 10^{38} \text{ erg s}^{-1}$). In a recent paper Crain et al. (2010) showed that disc galaxies in simulations develop gaseous haloes with an associated X-ray luminosity that is in good agreement with the observational constraints. They argue that this lower X-ray luminosity is due to the density profile of the hot gas not following that of the dark matter and being much less centrally concentrated as a result of energy injection from SNe. Similarly, we can compute X-ray luminosities for our assumed hot gas haloes. To do this we integrate the emissivity over the volume of the halo in the 0.3-2 keV band (see Navarro et al. 1995 for a prescription to do this for SPH simulations). For our galaxy models Z1A4, G3h and MBh we find $L_X = 2, 1$ and $10 \times 10^{38} \text{ erg s}^{-1}$, respectively. We thus conclude that even our maximal gaseous haloes are not in conflict with X-ray observations.

We have used MW-like galaxy models including a gaseous halo in a series of binary merger simulations. We have run all mergers both with and without galactic winds using the ‘constant wind’ model of Springel & Hernquist (2003), where the mass-loss rate carried by the winds is proportional to the SFR and the wind speed is constant. However, this model has some deficiencies as the wind speed for low mass galaxies is the same as for high mass galaxies

resulting in too much heating for low mass systems. More recent models have been developed that attempt to overcome these problems and present a more realistic match to observed quantities, e.g. momentum driven winds (Oppenheimer & Davé 2006), in which the mass loading factor and wind velocity are functions of the internal galaxy velocity dispersion. However, since our study focussed on equal mass galaxies, and our galaxies do not change their internal velocity dispersions significantly over the course of the simulation, we doubt that introducing such scalings would significantly effect our results.

We have studied the impact of a gaseous halo and stellar winds on the SFR using four ‘fiducial’ runs: without gaseous halo and without winds (G3G3), without gaseous halo but with winds (G3G3w), without winds but with a gaseous halo (G3G3h) and with both winds and gaseous halo (G3G3wh). We found that in simulations without a gaseous halo, the maximum SFR during a starburst is ~ 30 times larger than that of the constituent galaxies evolved in isolation. When a gaseous halo is included, this enhancement is much smaller (factor of ~ 5). The reason for this is the higher SFR of the isolated systems when a cooling halo is included. Isolated systems without a hot halo, however, consume most of their gas early on in the simulation, such that the SFR is very low by the time of the starburst in the merger simulation. We also found that when stellar winds are included, the starburst is spread over a much larger time interval than in simulations without winds. This is because the winds eject cold gas from the centre of the galaxy into the hot halo. From there it can cool and accrete back to the centre resulting in a higher SFR at late times in the case without winds.

Furthermore, we studied the effects of the gaseous halo on the starburst efficiency, which we defined as the stellar mass which formed due to the burst divided by the mass of cold gas in the galaxies just before the merger. For the G3G3 run we found an efficiency of $e = 0.68$ while for G3G3w it is only $e = 0.45$, showing that the efficiency depends on the wind model and its parameters. The presence of a gaseous halo reduces the efficiency in G3G3h to $e = 0.51$. In addition, the SFR after the burst is lower than the SFR of the constituent galaxies evolved in isolation, resulting in a remnant stellar mass that is lower than that of the two isolated galaxies. This occurs for two reasons: first, the specific angular momentum of the hot gas after the merger is higher than that of the isolated systems, due to the acquisition of orbital angular momentum. This leads to a higher centrifugal barrier and thus to a lower accretion rate and SFR. Second, due to shocks that occur during the merger, the temperature of the gaseous halo in the merger case is higher than in the isolated case, leading to a longer cooling time and a lower SFR. The fact that two non-merging galaxies can have a larger stellar mass than if they had merged poses a challenge for semi-analytic models, which generally assume that a merger always leads to enhanced star formation.

We have also studied how the starburst efficiency depends on the initial cold gas fraction in the progenitors and found that without a gaseous halo, it decreases with increasing gas fraction. Higher gas fractions imply a lower stellar mass, which suppresses the formation of a stellar bar that can remove angular momentum from the gas Hopkins et al. (2009a). If a hot gaseous halo is present, however, the starburst efficiency increases with increasing gas fraction, as the

initial dense gas disc is replaced by accreting gas from the halo which is spatially much more extended. Systems with higher initial gas fractions retain more of their initial dense gas at the time of the merger which then leads to a more efficient burst. If winds are also included, the formation of massive stellar discs in very gas rich galaxies is prevented such that the starburst efficiency is again decreased.

Our simulations are closely related to prior studies on the efficiency of starbursts in binary galaxy mergers, and it is important to compare the results of our simulations without gaseous haloes or winds to those obtained by Cox et al. (2008) and Hopkins et al. (2009a), which also neglected these effects. Using the same progenitor galaxies (G3) but a different star formation model, Cox et al. (2008) find a starburst efficiency for G3G3 of $e = 0.5$. However, in the definition of e , they have used the gas fraction at the start of the simulation rather than just before the burst. As the gas fraction decreases until the time of the burst, the efficiency would increase to $e = 0.67$ for our definition. This is in excellent agreement with our value of $e = 0.68$. Hopkins et al. (2009a) used a large suite of simulations to develop an analytic model for the burst efficiency. For our orbit, mass ratio and gas fraction this model predicts an efficiency of $e = 0.74$. However, this small difference ($\lesssim 10\%$) is expected, as the simulations used by Hopkins et al. (2009a) to tune their model use a ‘softer’ EOS ($q = 0.25$; see Springel et al. 2005 for details). As a result, more gas can lose angular momentum and fall to the centre during the starburst, increasing the starburst efficiency.

We have also addressed the question of how the gaseous halo affects the morphology of merger remnants. Analysing the systems ~ 3 Gyr after the final coalescence, we found that when a gaseous halo is included in the initial conditions, the bulge-to-total ratio is decreased. This is a consequence of cooling and accretion of gas from the halo into a cold gas disc at the centre which subsequently forms stars, leading to a new stellar disc. However, all remnants remain bulge-dominated ($B/T \sim 0.8-0.9$). Furthermore, we found that the presence of a gaseous halo affects the surface brightness profiles of the remnants. While systems with no gaseous halo deviate from the observed $r^{1/4}$ profile at small scales, systems with a hot halo match the observed profile. The reason is the new stellar disc which leads to a higher surface density at the centre.

A kinematic analysis of the merger remnants showed that if the progenitor galaxies contain only $\sim 20\%$ cold gas and no gaseous halo, our chosen orbit leads to a remnant which is slowly rotating and only supported by velocity dispersion. When a gaseous halo is included, however, the rotational support of the remnant strongly increases. This can be also explained by the presence of a massive stellar disc in the centre that forms after the merger. The rotation of this disc contributes to the total rotational support in a mass-weighted average and leads to a larger potential at the centre, which causes ‘old’ stars to fall towards the centre and to increase their rotational velocity due to conservation of angular momentum. We have further studied the impact of the gaseous halo on the isophotal shape of the remnants and found that including a gaseous halo leads to remnants that are more discy on average. We found that both the kinematic structure and the isophotal shape of the remnants with a gaseous halo agree very well with observed ellipticals.

Studying the effects of cold gas fraction in progenitor galaxies on the kinematic structure of major merger remnants, Cox et al. (2006b) conclude that in order to form realistic low-luminosity elliptical galaxies in merger simulations, the progenitor galaxies must have high gas fractions of $\sim 40\%$. Our results confirm that an ample supply of cold gas must be present at the centre of the merger remnant, but suggest that the progenitor galaxies need not have such high gas fractions. Instead, accretion from a hot gas halo, which is expected to be present, can provide the necessary supply of cold gas.

As the hot gas in the halo is expected in all progenitor galaxies it has to be considered in all simulations that aim to reproduce typical observed galaxies. Our simulations and analysis show that by employing a more realistic model for the progenitor disc galaxy including this component it is possible to explain several aspects of observed elliptical galaxies through equal mass mergers of discs, such as an $r^{1/4}$ stellar surface brightness profile at small scales and the formation of fast rotators which dominate the local early-type population (e.g. Emsellem et al. 2011). However, this leads to the opposite problem for massive ellipticals: if a hot gaseous halo (expected in all progenitor galaxies) always leads to a rotationally supported system, how can slow rotators form? Traditionally they have been expected to form only in disc mergers with mass ratios of 1:1 or 1:2 (see Jesseit et al. 2009; Bois et al. 2010, for a detailed discussion). This is related to the problem of how elliptical galaxies can have low SFRs and red colours as observed, if a gaseous halo leads to the continuous accretion of cold gas and thus to ongoing SF. In contrast to observed elliptical galaxies the remnants in our simulations including the gaseous halo have relatively high SFRs and young stellar populations. This general problem has been discussed by Naab & Ostriker (2009) who conclude that elliptical galaxies can only form through a merger of typical disc galaxies if they have merged more than 3–4 Gyr ago and star formation is quenched afterwards. Moreover, there is evidence that dissipation is important in the formation of low-mass ellipticals, but less so in massive ones (e.g. De Lucia et al. 2006; Khochfar & Burkert 2006; Guo & White 2008; De Lucia & Blaizot 2007; Oser et al. 2010). Therefore we need a process that is more effective at high masses.

In order to solve these problems, there must be a process that prevents the hot gas in massive haloes from cooling as efficiently as we would otherwise expect, i.e., a source of heating that is more effective in massive haloes. There have been various suggestions for what this process might be, for example, heating by radio jets from AGN (Croton et al. 2006; Bower et al. 2006; Somerville et al. 2008b), or gravitational heating by substructure or clumpy accretion (Khochfar & Ostriker 2008; Dekel & Birnboim 2008; Johansson et al. 2009b). The former fits in nicely with the observed correlation between slow rotation, boxy isophotes, and radio detections. In addition, mergers may also fuel ‘bright mode’ AGN activity associated with the rapid accretion of cold gas into the galactic nucleus and onto a central supermassive black hole. This activity may be able to drive winds that remove cold gas from the galaxy, resulting in a lower SFR and older stellar populations in the remnant. However, if star formation is quenched immediately after the merger, then a prominent stellar disk will not be able to reform, and

the remnant will have neither have ‘extra light’ in the centre nor rotation. In this case, fast rotators could still form from disc mergers with high mass ratios (e.g. Barnes 1998; Naab & Burkert 2003). Another possibility is that AGN feedback is delayed, so that the merger remnant can form a disc before the cold gas is removed.

Moreover, we have not included cosmological accretion from outside the initial virial radius of the halo, which will be very significant at high redshift ($z > 1$). The radiative cooling model used in our simulation assumes a primordial mixture of hydrogen and helium and does not depend on the metallicity of the gas. This could lead to higher cooling rates resulting in larger SFRs such that even a less massive halo would cool relatively quickly. We have only simulated binary mergers, although multiple subsequent mergers are common in the Universe. Furthermore our simulations only consider one mass ratio (equal mass) and disc progenitors. Finally our study employs only one orbit. Thus, a full prediction of the demographics of early type galaxies (merger remnants) will require a self-consistent treatment of cosmological accretion, accretion from hot haloes, and feedback from stars and AGN.

ACKNOWLEDGEMENTS

We thank Hans-Walter Rix, Glenn van de Ven, Arjen van der Wel, Volker Springel, Tom Abel, and Simon White for enlightening discussions and useful comments on this work. We also thank Volker Springel for providing the code used as a basis to create the initial conditions. The numerical simulations used in this work were performed on the PIA and THEO clusters of the Max-Planck-Institut für Astronomie and on the PanStarrs2 clusters at the Rechenzentrum in Garching. BPM thanks the Space Telescope Science Institute for hospitality and financial support for his visit. BPM also acknowledges a travel grant from the German Research Foundation (DFG) within the framework of the excellence initiative through the Heidelberg Graduate School of Fundamental Physics.

REFERENCES

Abadi M. G., Navarro J. F., Steinmetz M., Eke V. R., 2003, *ApJ*, 597, 21

Barden M., et al., 2005, *ApJ*, 635, 959

Barnes J. E., 1988, *ApJ*, 331, 699

Barnes J. E., 1998, in R. C. Kennicutt Jr., F. Schweizer, J. E. Barnes, D. Friedli, L. Martinet, & D. Pfenniger ed., Saas-Fee Advanced Course 26: Galaxies: Interactions and Induced Star Formation Dynamics of Galaxy Interactions. pp 275–+

Barnes J. E., 2002, *MNRAS*, 333, 481

Barnes J. E., Hernquist L., 1996, *ApJ*, 471, 115

Barnes J. E., Hernquist L. E., 1991, *ApJL*, 370, L65

Barton Gillespie E., Geller M. J., Kenyon S. J., 2003, *ApJ*, 582, 668

Bekki K., 1998, *ApJL*, 502, L133+

Bekki K., Shioya Y., 1997, *ApJL*, 478, L17+

Bell E. F., de Jong R. S., 2001, *ApJ*, 550, 212

Bell E. F., et al., 2008, *ApJ*, 680, 295

Bell E. F., McIntosh D. H., Katz N., Weinberg M. D., 2003, *ApJ*, 585, L117

Bender R., 1988, *A&A*, 193, L7

Bender R., Doebeleiner S., Moellenhoff C., 1988, *A&AS*, 74, 385

Bender R., Nieto J., 1990, *A&A*, 239, 97

Bender R., Surma P., Doebeleiner S., Moellenhoff C., Madejsky R., 1989, *A&A*, 217, 35

Bendo G. J., Barnes J. E., 2000, *MNRAS*, 316, 315

Benson A. J., 2005, *MNRAS*, 358, 551

Benson A. J., Bower R. G., Frenk C. S., White S. D. M., 2000, *MNRAS*, 314, 557

Binney J., 2005, *MNRAS*, 363, 937

Binney J., Tremaine S., 1987, Galactic dynamics. Princeton, NJ, Princeton University Press, 1987, 747 p.

Bois M., et al., 2010, *MNRAS*, 406, 2405

Bournaud F., Jog C. J., Combes F., 2005, *A&A*, 437, 69

Bower R. G., Benson A. J., Malbon R., Helly J. C., Frenk C. S., Baugh C. M., Cole S., Lacey C. G., 2006, *MNRAS*, 370, 645

Bridge C. R., Carlberg R. G., Sullivan M., 2010, *ApJ*, 709, 1067

Bridge C. R., et al., 2007, *ApJ*, 659, 931

Brook C. B., Kawata D., Gibson B. K., Freeman K. C., 2004, *ApJ*, 612, 894

Bullock J. S., Dekel A., Kolatt T. S., Kravtsov A. V., Klypin A. A., Porciani C., Primack J. R., 2001, *ApJ*, 555, 240

Bullock J. S., Johnston K. V., 2005, *ApJ*, 635, 931

Burkert A., Naab T., Johansson P. H., Jesseit R., 2008, *ApJ*, 685, 897

Cappellari M., et al., 2007, *MNRAS*, 379, 418

Cappellari M., et al., 2011, *MNRAS*, pp 269–

Carlberg R. G., 1986, *ApJ*, 310, 593

Cavaliere A., Fusco-Femiano R., 1976, *A&A*, 49, 137

Conselice C. J., Rajgor S., Myers R., 2008, *MNRAS*, 386, 909

Conselice C. J., Yang C., Bluck A. F. L., 2009, *MNRAS*, 394, 1956

Cox T. J., Di Matteo T., Hernquist L., Hopkins P. F., Robertson B., Springel V., 2006a, *ApJ*, 643, 692

Cox T. J., Dutta S. N., Di Matteo T., Hernquist L., Hopkins P. F., Robertson B., Springel V., 2006b, *ApJ*, 650, 791

Cox T. J., Jonsson P., Primack J. R., Somerville R. S., 2006c, *MNRAS*, 373, 1013

Cox T. J., Jonsson P., Somerville R. S., Primack J. R., Dekel A., 2008, *MNRAS*, 384, 386

Cox T. J., Primack J., Jonsson P., Somerville R. S., 2004, *ApJL*, 607, L87

Crain R. A., McCarthy I. G., Frenk C. S., Theuns T., Schaye J., 2010, *MNRAS*, 407, 1403

Croton D. J., Springel V., White S. D. M., De Lucia G., Frenk C. S., Gao L., Jenkins A., Kauffmann G., et al., 2006, *MNRAS*, 365, 11

Dasyra K. M., Tacconi L. J., Davies R. I., Genzel R., Lutz D., Naab T., Burkert A., Veilleux S., Sanders D. B., 2006, *ApJ*, 638, 745

Davies R. L., Efstathiou G., Fall S. M., Illingworth G., Schechter P. L., 1983, *ApJ*, 266, 41

Davis M., Efstathiou G., Frenk C. S., White S. D. M., 1985, *ApJ*, 292, 371

de Jong R. S., 1996, *A&A*, 313, 45

De Lucia G., Blaizot J., 2007, *MNRAS*, 375, 2

De Lucia G., Springel V., White S. D. M., Croton D., Kauffmann G., 2006, *MNRAS*, 366, 499

de Zeeuw P. T., et al., 2002, *MNRAS*, 329, 513

Debuhr J., Quataert E., Ma C., 2011, *MNRAS*, 412, 1341

Debuhr J., Quataert E., Ma C., Hopkins P., 2010, *MNRAS*, 406, L55

Dekel A., Birnboim Y., 2008, *MNRAS*, 383, 119

Di Matteo T., Springel V., Hernquist L., 2005, *Nature*, 433, 604

Doyon R., Wells M., Wright G. S., Joseph R. D., Nadeau D., James P. A., 1994, *ApJL*, 437, L23

Eke V. R., Navarro J. F., Frenk C. S., 1998, *ApJ*, 503, 569

Emsellem E., et al., 2007, *MNRAS*, 379, 401

Emsellem E., et al., 2011, arXiv:1102.4444

Erb D. K., Steidel C. C., Shapley A. E., Pettini M., Reddy N. A., Adelberger K. L., 2006, *ApJ*, 646, 107

Faber S. M., et al., 1997, *AJ*, 114, 1771

Ferrarese L., van den Bosch F. C., Ford H. C., Jaffe W., O'Connell R. W., 1994, *AJ*, 108, 1598

Genzel R., et al., 2008, *ApJ*, 687, 59

Genzel R., Tacconi L. J., Rigopoulou D., Lutz D., Tecza M., 2001, *ApJ*, 563, 527

Gerhard O. E., 1981, *MNRAS*, 197, 179

Gingold R. A., Monaghan J. J., 1977, *MNRAS*, 181, 375

Governato F., et al., 2009, *MNRAS*, 398, 312

Governato F., et al., 2010, *Nature*, 463, 203

Governato F., Willman B., Mayer L., Brooks A., Stinson G., Valenzuela O., Wadsley J., Quinn T., 2007, *MNRAS*, 374, 1479

Guo Q., White S. D. M., 2008, *MNRAS*, 384, 2

Haardt F., Madau P., 1996, *ApJ*, 461, 20

Hansen S. H., Macciò A. V., Romano-Díaz E., Hoffman Y., Brüggen M., Scappapietra E., Stinson G. S., 2010, arXiv:1012.2870

Hernquist L., 1989, *Nature*, 340, 687

Hernquist L., 1990, *ApJ*, 356, 359

Hernquist L., 1992, *ApJ*, 400, 460

Hernquist L., 1993, *ApJ*, 409, 548

Hernquist L., Spergel D. N., Heyl J. S., 1993, *ApJ*, 416, 415

Hoffman L., Cox T. J., Dutta S., Hernquist L., 2009, *ApJ*, 705, 920

Hopkins P. F., Cox T. J., Dutta S. N., Hernquist L., Kormendy J., Lauer T. R., 2009b, *ApJS*, 181, 135

Hopkins P. F., Cox T. J., Younger J. D., Hernquist L., 2009a, *ApJ*, 691, 1168

Hopkins P. F., Hernquist L., Cox T. J., Di Matteo T., Robertson B., Springel V., 2006, *ApJS*, 163, 1

Hopkins P. F., Hernquist L., Cox T. J., Dutta S. N., Rothberg B., 2008, *ApJ*, 679, 156

Hopkins P. F., Hernquist L., Cox T. J., Keres D., Wuyts S., 2009d, *ApJ*, 691, 1424

Hopkins P. F., Lauer T. R., Cox T. J., Hernquist L., Kormendy J., 2009c, *ApJS*, 181, 486

Jesseit R., Cappellari M., Naab T., Emsellem E., Burkert A., 2009, *MNRAS*, 397, 1202

Jesseit R., Naab T., Peletier R. F., Burkert A., 2007, *MNRAS*, 376, 997

Jogee S., et al., 2009, *ApJ*, 697, 1971

Johansson P. H., Naab T., Burkert A., 2009a, *ApJ*, 690, 802

Johansson P. H., Naab T., Ostriker J. P., 2009b, *ApJL*, 697, L38

Jones C., Forman W., 1984, *ApJ*, 276, 38

Kartaltepe J. S., et al., 2007, *ApJS*, 172, 320

Kassin S. A., et al., 2007, *ApJL*, 660, L35

Katz N., Weinberg D. H., Hernquist L., 1996, *ApJS*, 105, 19

Kauffmann G., White S. D. M., Guiderdoni B., 1993, *MNRAS*, 264, 201

Kaufmann T., Bullock J. S., Maller A. H., Fang T., Wadsley J., 2009, *MNRAS*, 396, 191

Kaufmann T., Mayer L., Wadsley J., Stadel J., Moore B., 2006, *MNRAS*, 370, 1612

Kazantzidis S., Bullock J. S., Zentner A. R., Kravtsov A. V., Moustakas L. A., 2008, *ApJ*, 688, 254

Kennicutt Jr. R. C., 1998, *ApJ*, 498, 541

Kennicutt Jr. R. C., Roettiger K. A., Keel W. C., van der Hulst J. M., Hummel E., 1987, *AJ*, 93, 1011

Khochfar S., Burkert A., 2006, *A&A*, 445, 403

Khochfar S., Ostriker J. P., 2008, *ApJ*, 680, 54

Klypin A., Kravtsov A. V., Bullock J. S., Primack J. R., 2001, *ApJ*, 554, 903

Kormendy J., Bender R., 1996, *ApJL*, 464, L119+

Kormendy J., Fisher D. B., Cornell M. E., Bender R., 2009, *ApJS*, 182, 216

Krajnović D., et al., 2008, *MNRAS*, 390, 93

Krajnović D., et al., 2011, arXiv:1102.3801

Lake G., 1989, *AJ*, 97, 1312

Lake G., Dressler A., 1986, *ApJ*, 310, 605

Larson R. B., Tinsley B. M., 1978, *ApJ*, 219, 46

Lauer T. R., et al., 1995, *AJ*, 110, 2622

Lauer T. R., et al., 2005, *AJ*, 129, 2138

Li Z., Wang Q. D., Hameed S., 2007, *MNRAS*, 376, 960

Lin L., et al., 2008, *ApJ*, 681, 232

Lotz J. M., et al., 2008, *ApJ*, 672, 177

Lucy L. B., 1977, *AJ*, 82, 1013

Macciò A. V., Dutton A. A., van den Bosch F. C., 2008, *MNRAS*, 391, 1940

Makino N., Sasaki S., Suto Y., 1998, *ApJ*, 497, 555

Martin C. L., 1999, *ApJ*, 513, 156

Martin C. L., 2005, *ApJ*, 621, 227

Mastropietro C., Burkert A., Moore B., 2009, *MNRAS*, 399, 2004

Mastropietro C., Moore B., Mayer L., Wadsley J., Stadel J., 2005, *MNRAS*, 363, 509

Mathews W. G., Brighenti F., 2003, *ARA&A*, 41, 191

McGaugh S. S., 2005, *ApJ*, 632, 859

Mihos J. C., Hernquist L., 1994, *ApJL*, 425, L13

Mihos J. C., Hernquist L., 1996, *ApJ*, 464, 641

Mo H. J., Mao S., White S. D. M., 1998, *MNRAS*, 295, 319

Monaco P., Fontanot F., Taffoni G., 2007, *MNRAS*, 375, 1189

Monaghan J. J., 1992, *ARA&A*, 30, 543

Moster B. P., Macciò A. V., Somerville R. S., Johansson P. H., Naab T., 2010, *MNRAS*, 403, 1009

Moster B. P., Somerville R. S., Maulbetsch C., van den Bosch F. C., Macciò A. V., Naab T., Oser L., 2010, *ApJ*, 710, 903

Murante G., et al., 2004, *ApJL*, 607, L83

Murante G., Poglio E., Curir A., Villalobos A., 2010, ApJL, 716, L115

Naab T., Burkert A., 2003, ApJ, 597, 893

Naab T., Burkert A., Hernquist L., 1999, ApJL, 523, L133

Naab T., Jesseit R., Burkert A., 2006, MNRAS, 372, 839

Naab T., Ostriker J. P., 2009, ApJ, 690, 1452

Naab T., Trujillo I., 2006, MNRAS, 369, 625

Navarro J. F., Frenk C. S., White S. D. M., 1995, MNRAS, 275, 720

Negroponte J., White S. D. M., 1983, MNRAS, 205, 1009

Oppenheimer B. D., Davé R., 2006, MNRAS, 373, 1265

Oser L., Ostriker J. P., Naab T., Johansson P. H., Burkert A., 2010, ApJ, 725, 2312

Owen R. A., Warwick R. S., 2009, MNRAS, 394, 1741

Price D. J., 2007, PASA, 24, 159

Puech M., et al., 2008, A&A, 484, 173

Purcell C. W., Kazantzidis S., Bullock J. S., 2009, ApJ, 694, L98

Quinn P. J., Hernquist L., Fullagar D. P., 1993, ApJ, 403, 74

Rasmussen J., Sommer-Larsen J., Pedersen K., Toft S., Benson A., Bower R. G., Grove L. F., 2009, ApJ, 697, 79

Read J. I., Lake G., Agertz O., Debattista V. P., 2008, MNRAS, 389, 1041

Rix H., Carollo C. M., Freeman K., 1999, ApJL, 513, L25

Rix H., White S. D. M., 1990, ApJ, 362, 52

Robertson B., Bullock J. S., Cox T. J., Di Matteo T., Hernquist L., Springel V., Yoshida N., 2006a, ApJ, 645, 986

Robertson B., Cox T. J., Hernquist L., Franx M., Hopkins P. F., Martini P., Springel V., 2006b, ApJ, 641, 21

Rothberg B., Joseph R. D., 2006, AJ, 132, 976

Rupke D. S., Veilleux S., Sanders D. B., 2005, ApJS, 160, 115

Salpeter E. E., 1955, ApJ, 121, 161

Sanders D. B., Soifer B. T., Elias J. H., Madore B. F., Matthews K., Neugebauer G., Scoville N. Z., 1988, ApJ, 325, 74

Schwarzkopf U., Dettmar R.-J., 2000, A&A, 361, 451

Schweizer F., 1982, ApJ, 252, 455

Scorza C., Bender R., Winkelmann C., Capaccioli M., Macchetto D. F., 1998, A&AS, 131, 265

Sembach K. R., et al., 2003, ApJS, 146, 165

Shen S., Mo H. J., White S. D. M., Blanton M. R., Kauffmann G., Voges W., Brinkmann J., Csabai I., 2003, MNRAS, 343, 978

Shier L. M., Fischer J., 1998, ApJ, 497, 163

Sinha M., Holley-Bockelmann K., 2009, MNRAS, 397, 190

Somerville R. S., et al., 2008a, ApJ, 672, 776

Somerville R. S., Hopkins P. F., Cox T. J., Robertson B. E., Hernquist L., 2008b, MNRAS, 391, 481

Sommer-Larsen J., 2006, ApJL, 644, L1

Sommer-Larsen J., Götz M., Portinari L., 2003, ApJ, 596, 47

Springel V., 2000, MNRAS, 312, 859

Springel V., 2005, MNRAS, 364, 1105

Springel V., 2010, ARA&A, 48, 391

Springel V., Di Matteo T., Hernquist L., 2005, MNRAS, 361, 776

Springel V., Hernquist L., 2002, MNRAS, 333, 649

Springel V., Hernquist L., 2003, MNRAS, 339, 289

Springel V., Hernquist L., 2005, ApJL, 622, L9

Stewart K. R., Bullock J. S., Wechsler R. H., Maller A. H., 2009, ApJ, 702, 307

Stinson G., Bailin J., Couchman H., Wadsley J., Shen S., Brook C., Quinn T., 2010, MNRAS, 408, 812

Strickland D. K., Heckman T. M., Colbert E. J. M., Hoopes C. G., Weaver K. A., 2004, ApJS, 151, 193

Sun M., Voit G. M., Donahue M., Jones C., Forman W., Vikhlinin A., 2009, ApJ, 693, 1142

Toft S., Rasmussen J., Sommer-Larsen J., Pedersen K., 2002, MNRAS, 335, 799

Toomre A., 1977, in B. M. Tinsley & R. B. Larson ed., Evolution of Galaxies and Stellar Populations Mergers and Some Consequences. pp 401–+

Toomre A., Toomre J., 1972, ApJ, 178, 623

Tripp T. M., et al., 2003, AJ, 125, 3122

Tüllmann R., Pietsch W., Rossa J., Breitschwerdt D., Dettmar R., 2006, A&A, 448, 43

van den Bosch F. C., 2001, MNRAS, 327, 1334

van den Bosch F. C., Abel T., Croft R. A. C., Hernquist L., White S. D. M., 2002, ApJ, 576, 21

van Dokkum P. G., et al., 2004, ApJ, 611, 703

Velazquez H., White S. D. M., 1999, MNRAS, 304, 254

Villalobos Á., Helmi A., 2008, MNRAS, 391, 1806

Viola M., Monaco P., Borgani S., Murante G., Tornatore L., 2008, MNRAS, 383, 777

Wang Q. D., 2005, in R. Braun ed., Extra-Planar Gas Vol. 331 of Astronomical Society of the Pacific Conference Series, Extra-planar Diffuse Hot Gas Around Normal Disk Galaxies. pp 329–+

Wang Q. D., Chaves T., Irwin J. A., 2003, ApJ, 598, 969

White S. D. M., Rees M. J., 1978, MNRAS, 183, 341

Yoachim P., Dalcanton J. J., 2006, AJ, 131, 226

Younger J. D., Hayward C. C., Narayanan D., Cox T. J., Hernquist L., Jonsson P., 2009, MNRAS, 396, L66